Journal of Applied Pharmaceutical Science 2025. Article in Press
Available online at http://www.japsonline.com
DOI: 10.7324/JAPS.2026.249308
ISSN 2231-3354

Metabolomics and cheminformatics bioprospection of corn silk against key enzymes implicated in type 2 diabetes mellitus and its complications

Ayesha Akoonjee[1], Halimat Yusuf Lukman[1], Adedayo Ayodeji Lanrewaju[1], Raliat Abimbola Aladodo[2], Saheed Sabiu[1*]

[1]Department of Biotechnology and Food Science, Faculty of Applied Sciences, Durban University of Technology, Durban, South Africa.
[2]Department of Biochemistry, College of Pure and Applied Sciences, Kwara State University, Ilorin, Nigeria.

ARTICLE HISTORY

Received on: 25/03/2025
Accepted on: 14/07/2025
Available Online: XX

Key words:
Corn silk metabolites, metabolomics, molecular docking, molecular dynamics simulation, solvent variation, type 2 diabetes mellitus.

ABSTRACT

The rising prevalence of type 2 diabetes mellitus (T2DM) and the side effects of synthetic hypoglycemic agents underscore the need for new antidiabetic compounds. Corn silk (CS) is known for its antidiabetic properties, but its mechanism remains unclear. This study explored the potential of CS constituents in modulating six key enzymes linked to T2DM and its complications: alpha-amylase (AA), alpha-glucosidase (AG), aldose reductase (AR), dipeptidyl peptidase-4 (DPP-4), protein tyrosine phosphatase 1B (PTP1B), and sorbitol dehydrogenase (SDH), using computational techniques. Ultra-performance liquid chromatography-mass spectrometry identified 128 metabolites across three CS extracts (aqueous, hydro-ethanol, and ethanol) from premature and mature developmental stages. Mature CS had a higher metabolite abundance, particularly in the hydro-ethanolic extract. An insight into the structural interaction and binding energy calculations over a 120-ns molecular dynamics simulation identified R-7-butyl-6,8-dihydroxy-3-[(3E)-pent-3-en-1-yl]-3,4-dihydroisochromen-1-one (−40.30 kcal/mol), 1-O-vanilloyl-beta-D-glucose (−34.17 kcal/mol), (-)-11-hydroxy-9,10-dihydrojasmonic acid 11-beta-D-glucoside (−44.13 kcal/mol), p-coumaroyl malic acid (−34.40 kcal/mol), 2-hydroxydecanedioic acid (−19.71 kcal/mol), and (-)-11-hydroxy-9,10-dihydrojasmonic acid 11-beta-D-glucoside (−36.61 kcal/mol) with the highest negative binding free energy against AA, AG, AR, DPP-4, PTP1B, and SDH, respectively. Post-MD simulation confirmed the formation of more thermodynamically stable CS metabolites-enzyme complexes in comparison to the respective reference standard-enzyme complexes. Evidence from this study shows that CS metabolites possess potential inhibitory effects on the investigated targets and suggest that CS and its metabolites could be a potential alternative for managing T2DM.

Online First

1. INTRODUCTION

Type 2 diabetes mellitus (T2DM) is a significant global health issue, recognized as a chronic metabolic disorder that leads to high blood glucose levels due to inadequate insulin production and/or insulin resistance [1,2]. Prolonged exposure to T2DM or insufficient management can result in serious complications such as kidney disease, vision impairment, cardiovascular issues, heart attacks, strokes, nerve damage, skin disorders, and foot ulcers [2], potentially leading to death in severe instances [3]. In addition to these complications, T2DM places considerable physiological and psychological stress on individuals and creates a substantial financial burden on healthcare systems worldwide [4,5]. Although T2DM is classified as a noncommunicable disease, its rising prevalence across all demographics is alarming [6]. Currently, an estimated 537 million individuals globally are living with diabetes, with 90% diagnosed with T2DM [7].

The increased activity of alpha-amylase (AA) and alpha-glucosidase (AG) accelerates the breakdown of carbohydrates to simple sugars, resulting in a rapid influx of glucose in the bloodstream, contributing to postprandial hyperglycaemia [8]. Unlike AA and AG, dipeptidyl peptidase-4 (DPP-4) plays a role in breaking down glucagon-like peptide-1,

*Corresponding Author
Saheed Sabiu. Department of Biotechnology and Food Science, Faculty of Applied Sciences, Durban University of Technology, Durban, South Africa. E-mail: sabius @ dut.ac.za

© 2025 Ayesha Akoonjee *et al*. This is an open access article distributed under the terms of the Creative Commons Attribution 4.0 International License (https://creativecommons.org/licenses/by/4.0/).

an incretin hormone that stimulates insulin release and inhibits glucagon release. These two hormones are essential in regulating blood glucose levels [9]. Similarly, protein tyrosine phosphatase-1B (PTP1B) is involved in the dephosphorylation of insulin receptors and insulin receptor substrates, influencing the insulin signalling pathway [10]. In T2DM, elevated PTP1B activity hinders insulin signalling by excessively dephosphorylating insulin receptors, which results in decreased glucose uptake in cells, thus elevated blood glucose levels [11]. On the other hand, aldose reductase (AR) and sorbitol dehydrogenase (SDH) play crucial roles in the polyol pathway, a metabolic route responsible for converting glucose into sorbitol and sorbitol to fructose, respectively [12,13]. In T2DM, the activity of AR and SDH intensifies, resulting in the buildup of sorbitol and fructose within cells [14]. Accumulation of sorbitol and fructose can induce osmotic stress, causing cellular damage and dysfunction, thereby contributing to the development of secondary complications such as neuropathy, nephropathy, and diabetic retinopathy [15,16]. These six enzymes play crucial roles in the pathogenesis of T2DM or its related diabetic complications through various factors, not limited to glucose production and absorption, interference of insulin signalling, glucagon release, breakdown of glycogen, and increase of incretin concentration, accumulation of sorbitol, among others [17–22]. Therefore, effective modulation of the specific activity of these enzymes is crucial in the discovery and development of novel antidiabetic compounds and emerging target-based therapies [8,23].

The consistent maintenance of blood glucose levels using lifestyle changes, such as a healthy diet, regular physical exercise, consistent blood glucose monitoring, regular medical check-ups, and weight management, is often unattainable for many patients. This has necessitated reliance on synthetic medications to effectively manage diabetes and its complications [24]. While the potency of the synthetic oral hypoglycemic medications is undoubtable, the associated adverse side effects, compliance with a complex dosing schedule, and cost have undermined their application in clinical practice [24–26]. Therefore, the development of alternative or/and complementary therapeutics with promising antidiabetic potentials is imperative.

Due to the rich and diverse presence of metabolites, medicinal plants serve as a cogent source for the development of effective and culturally relevant therapeutic agents against several diseases, including T2DM [24,27]. Corn is popularly consumed in several parts of the world, including South Africa, with its cob and silk usually considered as waste. Corn silk (CS) is an underutilized corn part that consists of diverse phytochemicals, such as phenolic acids, flavonoids, carotenoids, sterols, tannins, volatile compounds, sugars, vitamins, minerals, polysaccharides, proteins, and peptides [25,28], many of which have contributed to its significant therapeutic properties [29,30]. Although CS is often discarded as a waste material [31], it has several pharmacological properties, including antioxidant, anti-inflammatory, diuretic, kaliuretic, anti-hyperlipidemic, anti-microbial, anti-cancer, anti-hypertensive, and antidiabetic [32], making it ethnopharmacologically relevant [27]. Studies have shown the antidiabetic potential of CS [33–37]; however, there is limited information on the mechanism of action behind its antidiabetic properties, particularly its relationship with the key enzymes implicated in T2DM pathogenesis.

Understanding the relationship between plant secondary metabolites, such as those present in CS, and enzymes implicated in the pathogenesis of T2DM can be useful for the development of targeted therapeutic approaches [38,39]. This will, in turn, contribute to the development of novel antidiabetic therapeutics and the emerging field of target-based therapies, which is expected to contribute to the effective management of T2DM [40]. To this extent, the study explored metabolomic profiling and computational techniques in the identification of CS secondary metabolites and their molecular interactions with key enzymes implicated in T2DM and its complications to identify possible novel compounds with antidiabetic potential.

2. METHODOLOGY

2.1. Corn silk collection and processing for the preparation of extracts

Fresh CS of a commonly consumed South African commercial corn hybrid ILHYB22 was collected at two developmental stages (premature and mature) at the Cedara College of Agriculture, KwaZulu-Natal, South Africa. The processing and preparation of CS from both developmental stages to produce three extracts [aqueous, hydro-ethanolic (50% ethanol), and ethanolic] were carried out as described in Figure 1 [41]. The powdered CS (raw) and the prepared extracts were stored (4°C) until needed [42].

2.2. Metabolomic profiling of corn silk

Ultra-performance liquid chromatography-mass spectrometry (UPLC-MS) analysis was performed on the raw and extracts (aqueous, hydro-ethanolic, and ethanolic) of mature and premature CS as previously reported [43,44]. A Water Synapt G2 quadruple time-of-flight mass spectrometer, connected to a Waters Acquity UPLC-combined with a photo diode array detector (Milford, MA, United States of America), was used to analyze the samples. Briefly, 2 g of each sample was subjected to ultrasonic-assisted extraction (SS-6508T, Sunshine, India) using a solvent system of 50% methanol and 0.1% formic acid for 24 hours at room temperature [43]. The samples were then centrifuged (mySPIN 12, Thermo Scientific, United States of America) for 5 minutes at 14,000 rpm, and the resulting supernatant in each case was used for further analysis. Acquisition and confirmation of data were performed using Masslynx 4.1, while MS-DIAL and MS-FINDER 2.0 software (RIKEN Center for Sustainable Resource Science: Metabolome Informatics Research Team, Kanagawa, Japan). Metaboanalyst (https://www.metaboanalyst.ca/MetaboAnalyst/) (accessed on 1 July 2022) was utilized for statistical analysis between the samples of CS, where principal component analysis, partial-least squares discriminant analysis, orthogonal partial-least squares discriminant analysis, and a hierarchical heat map were generated [44]. Relative abundance of the metabolites present in CS was performed based on peak height percentage [45].

2.3. Pharmacokinetics screening of corn silk metabolites

To identify orally bioavailable compounds and drug-likeness properties of the metabolites present in CS, virtual screening was conducted [46]. The Simplified Molecular

Online First

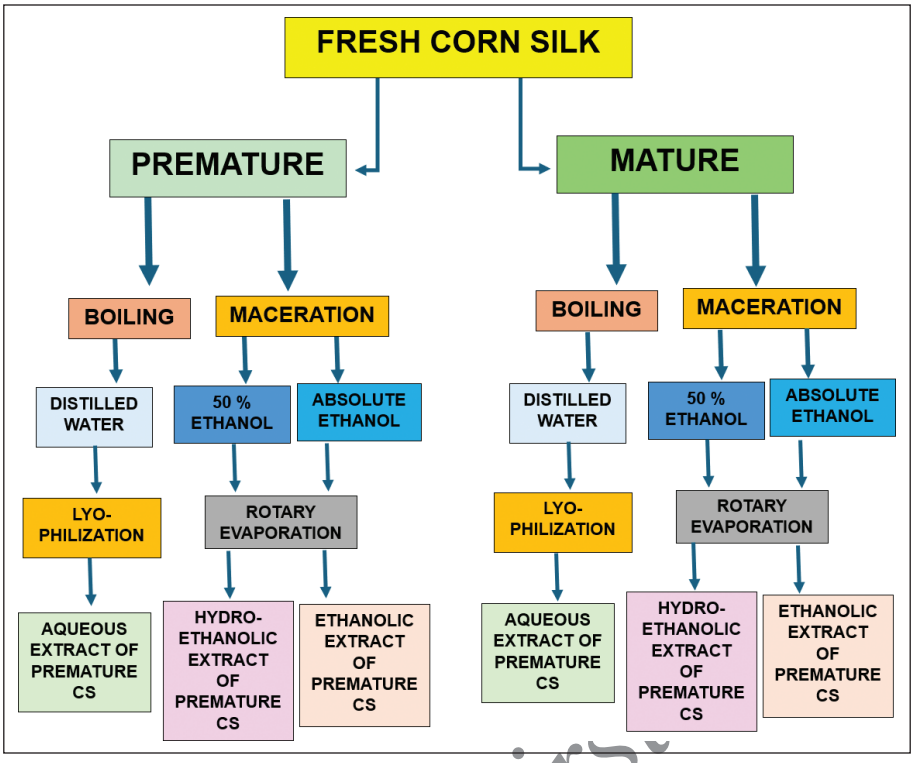

Figure 1. Preparation of aqueous, hydro-ethanolic, and ethanolic extracts of mature and premature corn silk (CS).

Online First

Input Line Entry System of the metabolites was obtained from the PubChem database (https://pubchem.ncbi.nlm.nih.gov/; accessed on 30 July 2022) and input into the SwissADME server (http://www.swissadme.ch/; accessed on 30 July 2022). Compounds with ≤ 2 violations of the Lipinski's rule (molecular weight ≤ 500 g/mol, < 5 hydrogen bond donors, ≤ 10 hydrogen bond acceptors, and partition coefficient Log p < 5) were selected for subsequent analysis. Molecular docking of corn silk metabolites against the investigated diabetes enzymes

Following pharmacokinetic screening, the identified metabolites and selected enzymes were subjected to molecular docking. The X-ray crystal structures of the six enzymes namely: AA (protein data bank (PDB) ID 4W93), AG (3W37), AR (3RX3), DPP-4 (1WCY), PTP1B (1SUG), and SDH (1PL8), were obtained from Research Collaboratory for Structural Bioinformatics Protein Protein Data Bank (https://www.rcsb.org/; accessed 1 September 2022). The enzymes were prepared using USCF Chimera v 1.16 [47]. The 3D conformers of the metabolites and the reference standards (acarbose for AA and AG, epalrestat for AR, ursolic acid for PTP1B, sitagliptin for DPP-4, and 4-[2-1R-hydroxy-ethyl)-pyrimidin-4-yl]piperazine-1-sulfonic acid dimethylamide for SDH) were obtained from PubChem (https://pubchem.ncbi.nlm.nih.gov/; accessed 1 September 2022) and subsequently optimized on USCF Chimera v 1.16 by addition of Gasteiger charges and nonpolar hydrogen atoms [21]. Identification of grid box coordinates (x-y-z) and grid box side (x-y-z) of the native ligand for each enzyme was determined on UCSF Chimera v 1.16. These were then used to dock the CS metabolites to the active site of the enzymes using the Autodock Vina Plugin on Chimera V1.16 [21]. To prevent pseudo-positive binding conformations, the docking protocol was validated as previously detailed [48] by measuring the root mean square deviation (RMSD) of docked ligands from the reference pocket bearing the native ligands in the co-crystal structures of AA, AG, AR, DPP-4, PTP1B, and SDH (Fig. 2a-f, respectively), following optimal superimposition. The RMSD of the docked ligands from the native inhibitor in the 3D structures of all six enzymes was 0.5 Å, which indicates similar binding orientation, ultimately validating the protocol employed.

2.4. Molecular dynamics (MD) simulation of corn silk metabolites against the investigated diabetes enzymes

After validating the docking protocol, the five complexes exhibiting the most favorable poses (indicated by the lowest docking scores) for each enzyme were chosen for further investigation through a 120-nanosecond molecular dynamics simulation, as previously described [49]. The simulation utilized the GPU force field within the AMBER 18 software, specifically employing the Force Field 18SB variant. The atomic partial charges for the compounds were derived using the restrained electrostatic potential and general amber force field methods from ANTECHAMBER. The leap module of AMBER 18 was employed to neutralize the system by adding hydrogen atoms along with Na+ and Cl- counter ions. The residues were designated as 1–495, 1–913, 1−315, 1–729, 1–299, and 1–356 for AA, AG, AR, DPP-4, PTP1B, and SDH, respectively. Each system was then implicitly positioned within an orthorhombic box of TIP3P water molecules, ensuring that all atoms were within 8Å of any edge of the box. The simulation was conducted using

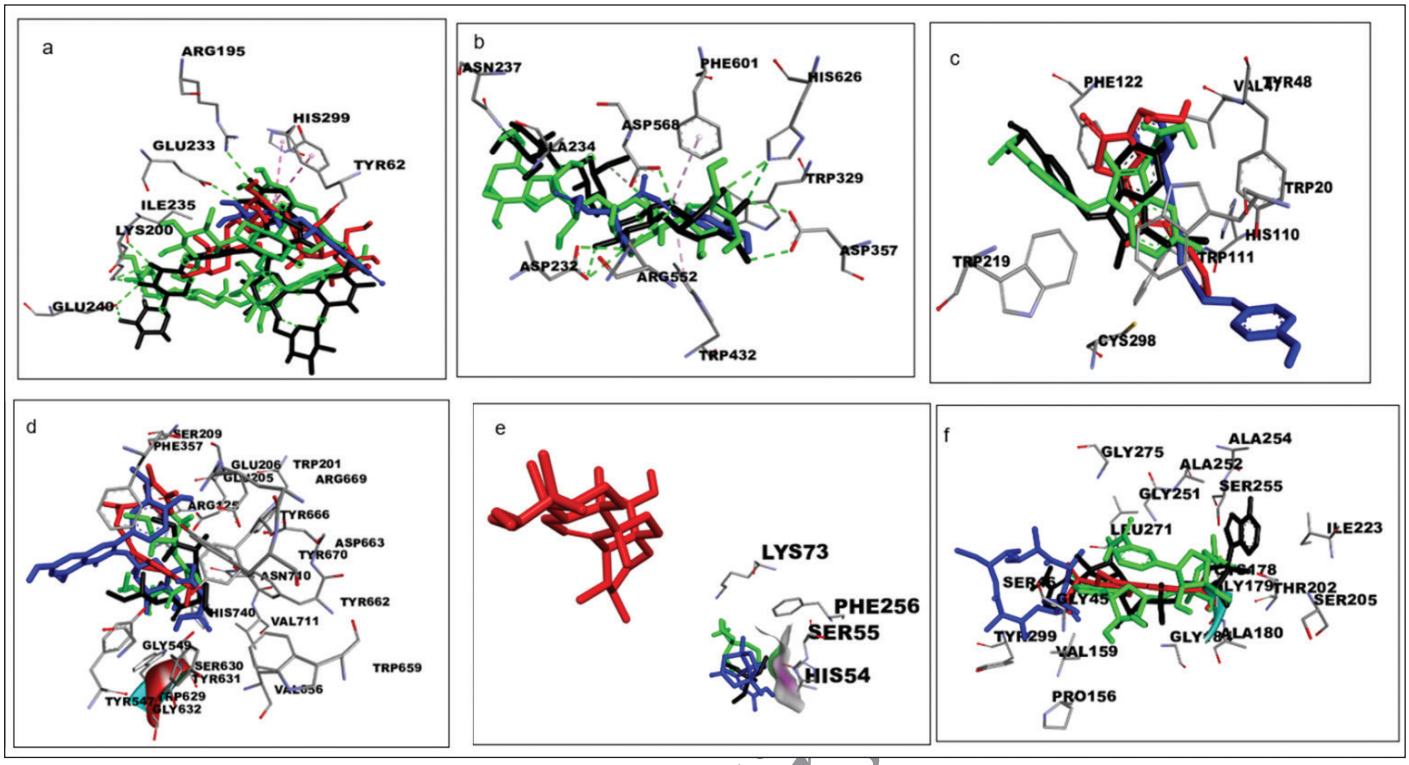

Figure 2. Superimposition on co-crystallized structure of a) alpha amylase: native ligand (black), superimposed docked native ligand (green), reference standard (red), and compound with the highest docking score (blue). Root mean square deviation (RMSD) value of 0.5 Å. Grid box co-ordinates: centre (X = −11, Y = 4, Z = −22) and size (X = 20, Y = 18, Z = 13); b) alpha glucosidase: native ligand (black), superimposed docked native ligand and standard (green) and compound with highest docking score (blue). RMSD value of 0.5 Å. Grid box co-ordinates: centre (X = 0.2, Y = −3, Z = −23) and size (X = 11, Y = 22, Z = 12); c) aldose reductase: native ligand (black), superimposed docked native ligand (green), reference standard (red), and compound with highest docking score (blue). RMSD value of 0.5 Å. Grid box co-ordinates: centre (X = −10, Y = 9, Z = 17) and size (X = 11, Y = 22, Z = 12); d) dipeptidyl peptidase 4: native ligand (black), superimposed docked native ligand (green), reference standard (red), and compound with highest docking score (blue). RMSD value of 0.5 Å. Grid box co-ordinates: centre (X = 56, Y = 62, Z = 35) and size (X = 13, Y = 10, Z = 7); e) protein tyrosinase phosphatase-1B: native ligand (black), superimposed docked native ligand (green), reference standard (red) and compound with highest docking score (blue). RMSD value of 0.5 Å. Grid box co-ordinates: centre (X = 44, Y = −3, Z = −4) and size (X = 7, Y = 6, Z = 7) and f) sorbitol dehydrogenase: native ligand (black), superimposed docked native ligand (green), reference standard (red) and compound with highest docking score (blue). RMSD value of 0.5 Å. Grid box co-ordinates: centre (X = 97, Y = 31, Z = 26) and size (X = 9, Y = 15, Z = 13).

Online First

the SHAKE algorithm from the Leap module to restrict the expansion of all chemical bonds, including those of hydrogen atoms. Each simulation step was set at 2 femtoseconds, and an SPFP precision model was utilized. The simulations adhered to the isobaric-isothermal ensemble, featuring randomized seeding, with the Berendsen barostat maintaining a constant pressure of 1 bar, a pressure-coupling constant of 2 ps, a temperature of 300 K, and a Langevin thermostat with a collision frequency of 1.0 ps. Post-dynamics data [RMSD, root mean square fluctuation (RMSF), radius of gyration (ROG), solvent accessible surface (SASA), and number of hydrogen bonds] were computed [50]. The binding free energy (ΔG_{bind}) was calculated using the Molecular Mechanics/GB Surface Area (MM/GBSA) method, wherein ΔG_{bind} was averaged over 120,000 snapshots extracted from the 120 ns trajectory [51]. Equations 1–5 depict the formula for the calculation of the average ΔG_{bind} for each molecular species (complex, ligand, and protein):

$$\Delta G_{bind} = E_{gas} + G_{sol} - TS \quad (1)$$

$$\Delta G_{bind} = G_{complex} - G_{receptor} - G_{ligand} \quad (2)$$

$$E_{gas} = E_{int} + E_{vdw} + E_{ele} \quad (3)$$

$$G_{sol} = G_{GB} + G_{SA} \quad (4)$$

$$G_{SA} = \gamma SASA \quad (5)$$

The complexes' (ligand-receptor) interaction at the active site of each enzyme was examined at 0 ns, 60 ns, and 120 ns using Discovery Studio version 21.1.1 [52].

2.5. Quantum chemical calculations

The molecular characteristics of the lead compounds were predicted using density functional theory (DFT) via quantum chemical calculations. The widely used 6-31 + G(d,p) basis set combined with the Becke3-Lee–Yang–Parr (B3LYP) method [53] was adopted to optimize the lead compounds using the Gaussian 16 suite of the CHPC, Cape Town, South Africa and the resulting files were then visualized using GaussView 6 software V 6.0.16. The study assessed the conceptual DFT (cDFT), namely the frontier molecular orbitals comprising the highest occupied molecular orbital (HOMO) and the lowest unoccupied molecular orbital (LUMO) [54], taking into consideration the Parr and Pearson interpretation of DFT and Koopmans' theorem [55]. Equations 6–13 were used to compute other chemical descriptors, including energy gap (ΔE),

ionization energy (I), electron affinity (A), chemical hardness (ŋ), softness (δ), electronegativity (χ), chemical potential (Cp), and global electrophilicity (ϖ).

$$\Delta E = E_{LUMO} - E_{HOMO} \quad (6)$$

$$I = -E_{LUMO} \quad (7)$$

$$A = -E_{HOMO} \quad (8)$$

$$\eta = \frac{\Delta E}{2} \quad (9)$$

$$\delta = \frac{1}{\eta} \quad (10)$$

$$\chi = \frac{(I+A)}{2} \quad (11)$$

$$Cp = -\chi \quad (12)$$

$$\varpi = \frac{\chi^2}{\Delta E} \quad (13)$$

2.6. Toxicity prediction

The top-performing compounds against the six targets were further analyzed for their toxicity profile by inputting their SMILES in the ProTox server (https://tox.charite.de/protox3/#; accessed on 7 July 2025) [56].

3. RESULTS

3.1. Metabolomic profiling of corn silk metabolites

The metabolites identified through UPLC-MS analysis (Supplementary Table S1) were confirmed on the chromatograms produced from MassLynx (Supplementary Figures S1–S4). Altogether, 128 metabolites (compounds C1–128) were identified in all the CS samples investigated. The highest amount of variation between the two developmental stages was 63.95 (41.1% in principal component 1% and 22.8% in principal component 2), with the compounds found to cluster majorly in two distinct positions (Fig. 3a). The top 15 compounds responsible for the high chemical diversity between the different developmental stages are presented in Figure 3b. Thirteen out of the 15 metabolites were found to be highly abundant in the mature CS, whereas C103 (Pandangolide 1) and C74 (3-hydroxysebaic acid) were more prevalent in the premature CS (Supplementary Table S1). The use of different extraction solvents produced variation in the type of metabolites extracted in both the premature and mature CS. Between the different samples of CS, there was 62.4% quantitative and qualitative variation of metabolites (42.1% in principal component 1 and 20.3% in principal component 2) (Fig. 4a). The top 15 metabolites responsible for the high chemical diversity between the eight samples of CS are presented in Figure 4b, where caffeoyl tartaric acid (C105) was the most variant between the samples. The top 15 CS metabolites were less abundant in the aqueous extracts of CS while out of the 15 metabolites which contributed to the highest variation between the extracts, a total of 5, 1, 4, 2, and 3 metabolites were highly abundant in raw premature CS, raw mature CS, hydro-ethanolic extract of premature CS, hydro-ethanolic extract of mature CS, and ethanolic extract of mature CS, respectively (Fig. 4b).

The relative abundance of the metabolites in the different samples of CS is presented in Supplementary Figure S5 (compounds C1–C65) and Supplementary Figure S6 (compounds C66–C128), as well as Supplementary Table S2. Majority of the metabolites were found to be more abundant

Online First

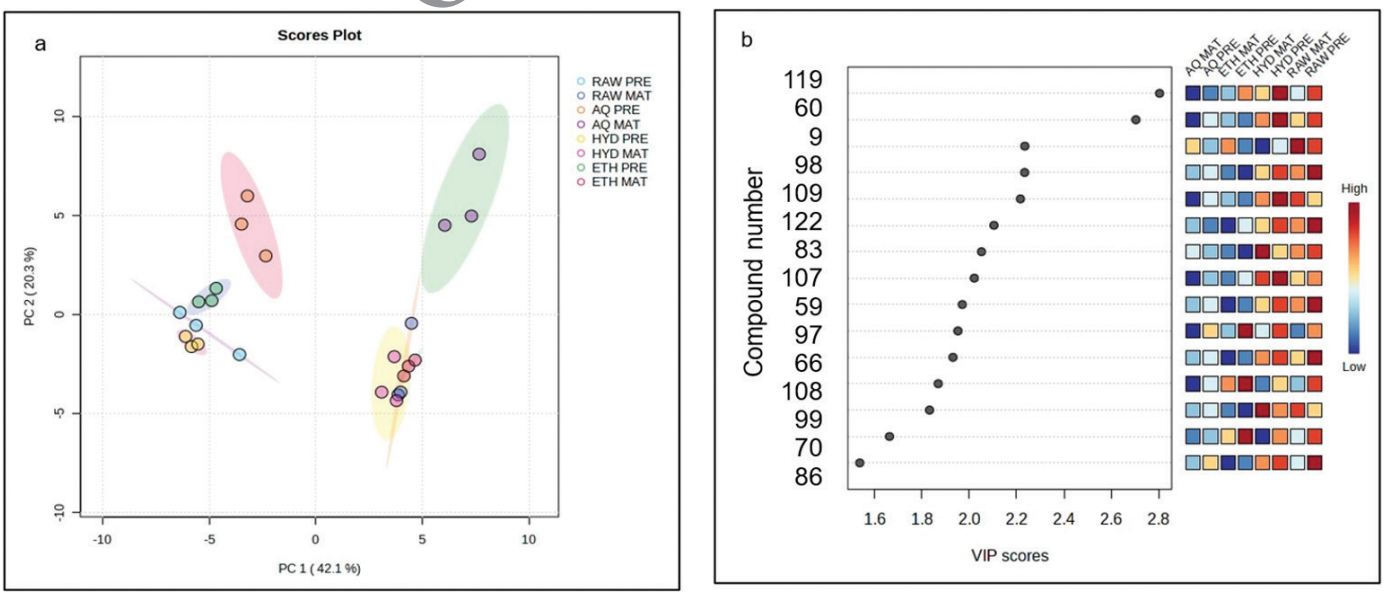

Figure 3. a) Principal component analysis plot of the percentage chemical diversity of metabolites between the two different developmental growth stages [premature (light green) and mature (light red) of corn silk; b) Orthogonal partial least squares-discriminant analysis (OPLS-DA) loadings plot of the top fifteen metabolites that were the most chemically diverse between the two developmental growth stages of corn silk with red showing high prevalence and blue showing low prevalence. PC: principal component, C105: tetradecanedioic acid, C51: methyl geranate, C73: UNPD230015, C26: diaportinic acid, C107: genistin, C82: diaportinol, C27: benzyl-O-beta-D-glucopyranoside, C103: pandangolide 1a, C74: 3-hydroxysebacic acid, C69: dodecanedioic acid, C106: (R)-7-butyl-6,8-dihydroxy-3-[(3E)-pent-3-en-1-yl]-3,4-dihydroisochromen-1-one, C118: ginsenoyne E, C104: 4-hydroxynonenal, C55: daldiniapyrone, and C121: UNPD205010.

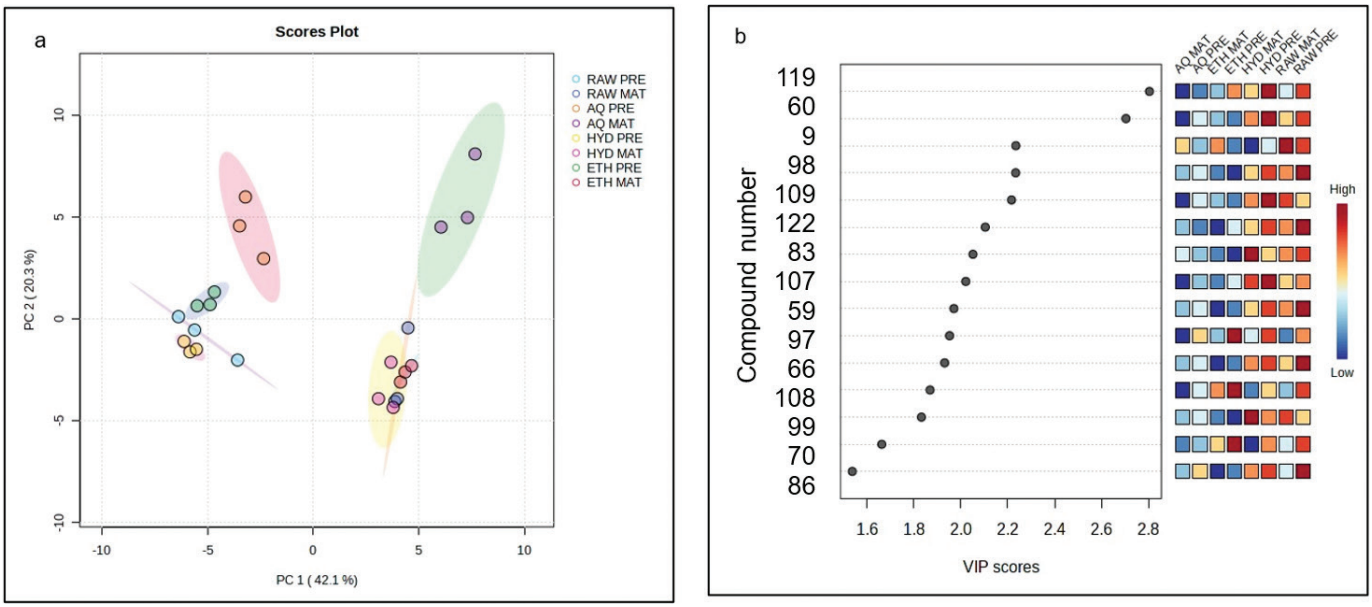

Figure 4. a). Principal component analysis scores plot of the percentage chemical diversity of metabolites (circle) between eight samples of CS [raw extract of premature CS (light blue), raw extract of mature CS (dark blue), aqueous extract of premature CS (orange), aqueous extract of mature CS (purple), hydro-ethanolic extract of premature CS (yellow), hydro-ethanolic extract of mature CS (pink), ethanolic extract of premature CS (green) and ethanolic extract of mature CS (light red)]; b) Partial least squares-discriminant analysis (PLS-DA) loading plot of the top 15 metabolites that were the most chemically diverse between the eight samples of CS with red showing high prevalence and blue showing low prevalence. AQ MAT: aqueous extract of mature CS, AQP; aqueous extract of premature CS, ETH MAT: ethanolic extract of mature CS, ETH PRE: ethanolic extract of premature CS, HYD MAT: hydro-ethanolic extract of mature CS, HYD PRE: hydro-ethanolic extract of premature CS, RAW MAT: raw extract of mature CS, RAW PRE: raw extract of premature CS. C119: caffeoyl tartaric acid, C60: quercitrin, C9: D-2-hydroxyglutaric acid, C98: 5,7,4'-trihydroxy-3'-methoxyflavone, C109: kaempferol 3-[2'''-acetyl-alpha-L-arabinopyranosyl-(1->6)-galactoside], C122: maysin 3'-methyl ether, C83: herbacetin 7-(6''-quinoylglucoside), C107: genistin, C59: apiin, C97: maysin, C66: UNPD19396, C108: p-coumaroyl malic acid, C99: quercetin 3-O-(6''-acetyl-glucoside), C70: kaempferitrin and C86: mirificin.

Online First

in the hydro-ethanolic extract of mature CS except compounds C3, C8, C21, C32, C33, C38, C42, C58, C105, and C124 (more abundant in aqueous extract of mature CS), compounds C1, C3, C8, C21, C32, C33, C92, C100, and C102 (more abundant in aqueous extract of premature CS) C47, C48, C61, C76, C82, C88, C89, C99, C103, and C106 (more abundant in ethanolic extract of mature CS), C36, C54, C70, C90, C96, C108, C125, C126, and C127 (more abundant in ethanolic extract of premature CS), C5 (more abundant in hydro-ethanolic extract of premature CS), and C65 (more abundant in raw extract of premature CS). The percentage yield of the 128 metabolites between the different samples of CS (aqueous, hydro-ethanolic, and ethanolic) extracts of premature and mature CS is presented in Supplementary Figure S7. Hydro-ethanolic extract of mature CS (37%) had the highest yield, followed by the hydro-ethanolic extract of premature CS (12%) and aqueous extract of premature CS (12%), with the raw sample of mature CS (5%) sample having the lowest yield.

3.2. Drug-likeness filtering of corn silk metabolites

Although several prediction analyses were considered (Lipinski, Veber, Mugge, and Egan rules) and all showed that most of the metabolites had ≤ 4 violations and demonstrated relatively good pharmacokinetic properties, including gastrointestinal absorption, blood-brain permeability, and were mostly nonphospho-glycoprotein substrates and noninhibitors of the cytochrome P450 isoenzymes. However, the most common Lipinski's rule of five (Ro5) was subsequently adopted for the screening of the metabolites. Out of the 128 metabolites identified in the different samples of CS, 110 passed Lipinski's Ro5, while 18 compounds exhibited more than 2 violations and were excluded from further analysis (Supplementary Table S3).

3.3. Molecular docking of corn silk metabolites against the investigated diabetes enzymes

Based on the docking scores, details of the top five CS metabolites with the investigated diabetes enzymes are provided in Table 1. Aesculin (AES), austricin (AUS), (6E)-1-(4-hydroxyphenyl)-7-phenylhepta-4,6-dien-3-one (HPH), (-)-11-hydroxy-9,10-dihydrojasmonic acid 11-beta-D-glucoside (HDJ), phaseic acid (PHA), and erythronolide B (ETB) had the highest negative docking scores against AA, AG, AR, DPP-4, PTP1B, and SDH, respectively (Table 1). The docking scores of the remaining 105 CS metabolites against the enzyme targets are presented in Supplementary Table S4.

3.4. Molecular dynamics simulation of top CS metabolites against the investigated diabetes enzymes

The ΔG_{bind} of the top five CS compounds against each of the investigated enzymes following a 120-ns MD simulation is presented in Table 2. Metabolites BHP (−40.30 kcal/mol), VBG (−34.17 kcal/mol), HDJ (−44.13 kcal/mol), CMA (−34.40 kcal/mol), HDA (−19.71 kcal/mol), and HDJ (−36.61 kcal/mol) had the highest negative ΔG_{bind} against AA, AG, AR, DPP-4, PTP1B, and SDH, respectively. Except for the AA-BHP complex, which had a lower negative ΔG_{bind} compared to AA-

Table 1. Molecular docking results of CS metabolites with the five highest negative docking score (best pose) and reference standards against each of the enzyme targets.

Compound number	Identity	Compound Abbreviation	Docking score (kcal/mol)
Alpha-amylase			
C31	Aesculin	AES	−8.1
C106	(R)-7-butyl-6,8-dihydroxy-3-[(3e)-pent-3-en-1-yl]-3,4-dihydroisochromen-1-one	BHP	−8.0
C88	Curvularol	CUR	−7.9
C14	(6e)-1-(4-hydroxyphenyl)-7-phenylhepta-4,6-dien-3-one	HPH	−7.8
C64	Austricin	AUS	−7.7
-	Acarbose*	ACA	−6.9
Alpha-glucosidase			
C64	Austricin	AUS	−7.8
C12	Glutaric acid	GTA	−7.7
C16	1-O-vanilloyl-beta-D-glucose	VBG	−7.5
C51	Methyl geranate	MGN	−7.4
C37	(-)-11-hydroxy-9,10-dihydrojasmonic acid 11-beta-D-glucoside	HDJ	−7.4
-	Acarbose*	ACA	−7.3
Aldose reductase			
C14	(6E)-1-(4-hydroxyphenyl)-7-phenylhepta-4,6-dien-3-one	HPH	−9.9
C106	(R)-7-butyl-6,8-dihydroxy-3-[(3E)-pent-3-en-1-yl]-3,4-dihydroisochromen-1-one	BHP	−8.6
C31	Aesculin	AES	−8.5
C64	Austricin	AUS	−8.5
C37	(-)-11-hydroxy-9,10-dihydrojasmonic acid 11-beta-D-glucoside	HDJ	−8.5
-	Epalrestat*	EPA	−6.3
Dipeptidyl peptidase-4			
C37	(-)-11-hydroxy-9,10-dihydrojasmonic acid 11-beta-D-glucoside	HDJ	−8.6
C119	Caffeoyl tartaric acid	CTA	−8.0
C106	(R)-7-butyl-6,8-dihydroxy-3-[(3E)-pent-3-en-1-yl]-3,4-dihydroisochromen-1-one	BHP	−7.8
C81	Phaseic acid	PHA	−7.8
C108	p-Coumaroyl malic acid	CMA	−7.7
-	Sitagliptin*	SGT	−6.2
Protein tyrosine phosphatase B			
C81	Phaseic acid	PHA	−6.0
C105	Tetradecanedioic acid	TDA	−5.8
C52	2-Hydroxydecanedioic acid	HDA	−5.4
C4	Methylisocitric acid	MCA	−5.2
C69	Dodecanedioic acid	DCA	−5.2
-	Ursolic acid*	URS	−5.2
Sorbitol dehydrogenase			
C72	Erythronolide B	ETB	−9.2
C111	(+)-Cnicin	CNI	−8.7
C100	Blennin D	BLD	−8.5
C37	(-)-11-hydroxy-9,10-dihydrojasmonic acid 11-beta-D-glucoside	HDJ	−8.4
C106	(R)-7-butyl-6,8-dihydroxy-3-[(3E)-pent-3-en-1-yl]-3,4-dihydroisochromen-1-one	BHP	−8.3
-	4-[2-1R-hydroxy-ethyl)-pyrimidin-4- yl] piperazine-1-sulfonic acid dimethylamide*	HPS	−5.0

*Reference standards

Online First

acarbose (−49.08 kcal/mol), others had higher negative ΔG_{bind} than their respective standards (Table 2).

3.4.1. Post-dynamic analysis of top CS metabolites against alpha-amylase

The alterations in structure and conformation resulting from the interactions of the top-ranked metabolites of CS with the enzymes during the simulation periods are presented in Tables 3 and Figures 5–10. All CS metabolites-AA complexes had higher average RMSD values than apo-AA (1.57 Å), except for AA-AES (1.52 Å), displaying the lowest average RMSD among the metabolite-AA complexes (Table 3). Following equilibration at 10 ns, RMSD of all AA complexes fluctuated between 1.10 Å and 2.25 Å throughout the remaining simulation, while only AA-CUR fluctuated close to 2.50 Å from 70 ns till the end of the simulation (Fig. 5a). Conversely, both apo-AA (0.94 Å) and AA-ACA (0.97 Å) exhibited lower mean RMSF values than all AA complexes, with the AA-CUR complex presenting the least RMSF value (0.70 Å) (Table 3). Additionally, the complexes displayed random fluctuations in RMSF between 0.5 Å and 2.5 Å, with major fluctuations observed in various residues, including 120–140, 180–200, 240–320, 340–400, 405–410, and 450–495, swaying between 0.5 Å and 5.75 Å (Fig. 5b). All AA-complexes exhibited lower mean ROG values compared to apo-AA, except CUR- (23.38 Å) and AUS-AA complexes (23.45 Å) (Table 3). After 5 ns, a stable ROG plot for all the bound complexes between 23.9 Å and 23.6 Å was observed except for ACA, which exhibited random fluctuations at 30, 80, and 100 ns (Fig. 5c). A marginal increase in the mean number of hydrogen bonds formed in the CS metabolites complexes relative to the apo-enzyme was observed [BHP (266.49), CUR (267.01), and

Table 2. Thermodynamic components of top 5 identified secondary metabolites present in CS against target enzymes.

(kcal/mol)					
Complex	**ΔE_{VdW}**	**ΔE_{elec}**	**ΔG_{gas}**	**ΔG_{solv}**	**ΔG_{bind}**
Alpha-amylase					
AES	−28.64 ± 4.67	−38.73 ± 14.93	−67.37 ± 15.14	39.07 ± 8.41	−28.31 ± 8.24
BHP	−36.06 ± 3.95	−48.13± 14.03	−85.20 ± 14.41	45.17 ± 7.85	−40.30 ± 7.35
CUR	−24.89 ± 3.08	−27.14 ± 6.24	−52.03 ± 5.91	22.88 ± 3.75	−29.15 ± 3.74
HPH	−28.16 ± 4.81	−14.85 ± 6.56	−43.00 ± 6.46	19.40 ± 4.34	−23.55 ± 5.30
AUS	−24.98 ± 3.25	−10.72 ± 9.37	−35.69 ± 10.80	17.24 ± 7.93	−18.45 ± 4.04
ACA	−51.81 ± 5.29	−132.83 ± 15.05	−184.60 ± 14.87	135.57 ± 10.04	−49.08 ± 7.99
Alpha-glucosidase					
AUS	−24.10 ± 3.30	−44.02 ± 23.29	−68.12 ± 23.36	46.91 ± 18.00	−21.21 ± 7.72
GTA	−26.16 ± 4.32	−31.61 ± 22.53	−57.78 ± 23.27	35.19 ± 13.17	−22.57 ± 12.05
VBG	−23.42 ± 3.54	−72.98 ± 14.48	−96.40 ± 14.00	62.22 ± 8.84	−34.17 ± 6.08
MGN	−11.98 ± 9.58	−7.45 ± 8.63	−18.21 ± 16.09	11.29 ± 9.94	−6.92 ± 7.00
HDJ	−27.81 ± 4.45	−52.92 ± 14.77	−80.73 ± 13.48	52.10 ± 9.52	−28.63 ± 5.74
ACA	−31.64 ± 5.13	−161.95 ± 22.72	−193.60 ± 23.49	177.05 ± 20.09	−16.54 ± 6.71
Aldose reductase					
HPH	−35.06 ± 3.18	−25.23 ± 7.03	−60.30 ± 8.03	26.16 ± 3.87	−34.13 ± 5.05
BHP	−47.41 ± 2.95	−19.07 ± 4.47	−66.49 ± 5.16	25.64 ± 3.38	−40.85 ± 3.44
AES	−43.04 ± 5.01	−27.19 ± 9.85	−70.23 ± 11.30	33.01 ± 5.68	−37.22 ± 8.40
AUS	−35.07 ± 3.27	−13.42 ± 11.84	−48.50 ± 12.88	17.47 ± 7.66	−31.02 ± 5.99
HDJ	−58.97 ± 4.97	−33.08 ± 8.12	−92.06 ± 10.51	47.92 ± 5.78	−44.13± 6.75
EPA	−21.18 ± 5.82	−9.73 ± 8.05	−30.91 ± 9.94	15.80 ± 6.48	−15.10 ± 5.02
Dipeptidyl peptidase-4					
HDJ	−16.28 ± 12.70	−20.99 ± 25.20	−37.27 ± 33.50	25.26 ± 23.85	−12.00 ± 10.42
CTA	−23.08 ± 3.41	−49.31 ±16.10	−72.39 ± 15.32	55.70 ± 12.05	−16.69 ± 4.72
BHP	−36.40 ± 4.65	−46.36 ± 12.31	−82.77 ± 13.24	49.54 ± 8.24	−33.22 ± 6.24
PHA	−27.98 ± 3.30	−51.07 ± 8.92	−79.06 ± 8.45	57.26 ± 6.46	−21.79 ± 4.06
CMA	−18.45 ± 3.76	-77.1195 ± 8.25	-95.58 ± 7.62	61.16 ± 5.38	-34.40 ± 4.17
HDJ	−39.63 ± 4.59	-254.13 ± 12.21	-293.75 ± 12.39	262.99 ± 11.01	-30.77 ± 4.71
Protein tyrosine phosphatase B					
PHA	−16.47 ± 5.83	−11.47 ± 8.38	−27.94 ± 11.01	19.30 ± 8.62	−8.64 ± 3.49
TDA	−20.88 ± 6.79	−18.80 ± 13.35	−39.68 ± 16.18	21.95 ± 11.27	−17.72 ± 6.72
HDA	−21.31 ± 4.27	−20.75 ± 10.38	−42.07 ± 11.85	22.36 ± 7.68	−19.71 ± 5.86
MCA	−16.76 ± 3.66	−29.90 ± 14.68	−46.66 ± 16.42	33.19 ± 12.75	−13.47 ± 4.53
DCA	−13.54 ± 7.80	−13.76 ± 10.83	−27.30 ± 15.28	14.77 ± 8.80	−12.52 ± 8.06
URS	−30.78 ± 3.51	−13.01 ± 6.23	−36.19 ± 6.89	20.15 ± 5.79	−16.03 ± 4.03
Sorbitol dehydrogenase					
ETB	−28.90 ± 3.75	−23.10 ± 14.35	−52.01 ± 15.71	31.37 ± 10.29	−20.63 ± 7.06
CNI	−27.87 ± 5.69	−22.19 ± 14.26	−50.06 ± 14.79	27.99 ± 9.04	−22.06 ± 7.03
BLD	−23.54 ± 5.45	−12.27 ± 7.63	−35.82 ± 10.79	17.13 ± 6.44	−18.69 ± 7.07
HDJ	−40.01 ± 6.01	−56.06 ± 9.90	−96.08 ± 13.13	59.46 ± 7.41	−36.61 ± 7.39
BHP	−32.12 ± 4.05	−35.79 ± 8.64	−67.92 ± 9.72	40.60 ± 5.70	−27.31 ± 5.25
HPS	−36.62 ± 5.69	−12.81 ± 6.22	−44.43 ± 9.35	8.19 ± 5.02	−34.24 ± 9.18

$\Delta E_{vdW:}$ Van der Waals energy; ΔE_{elec}: electrostatic energy; ΔE_{gas}: gas-phase free energy; ΔG_{solv} solvation free energy and ΔG_{bind}: total binding free energy. AES: aesculin; BHP: (R)-7-butyl-6,8-dihydroxy-3-[(3e)-pent-3-en-1-yl]-3,4-dihydroisochromen-1-one; CUR: curvularol; HPH: (6e)-1-(4-hydroxyphenyl)-7-phenylhepta-4,6-dien-3-one; AUS: austricin; ACA: acarbose; GTA: glutaric acid; VBG: 1-O-vanilloyl-beta-D-glucose; MGN: methyl geranate; HDJ: (-)-11-hydroxy-9,10-dihydrojasmonic acid 11-beta-D-glucoside; EPA: epalrestat; CTA: caffeoyl tartaric acid; PHA: phaseic acid; CMA: p-coumaroyl malic acid; SGT: sitagliptin; TDA: tetradecanedioc acid; HDA: 2-hydroxydecanedioic acid; MCA: methylisocitric acid; DCA: dodecanedioc acid; URS: ursolic acid; ETB: erythronolide B; CNI: cnicin; BLD: blennin D; HPS: 4-[2-1R-hydroxy-ethyl)-pyrimidin-4- yl]piperazine-1-sulfonic acid dimethylamide.

Online First

Table 3. Mean post-molecular dynamics parameters of top 5 identified metabolites of corn silk against the target enzymes.

Complexes	RMSD (Å)	RMSF (Å)	RoG (Å)	Number of H-Bonds	SASA (Å)
AA (apo-enzyme)	1.57 ± 0.15	0.94 ± 0.41	23.31 ± 0.09	266.48 ± 11.04	17,130.45 ± 426.56
AA-AES	1.52 ± 0.14	1.01 ± 0.50	23.28 ± 0.09	267.39 ± 10.24	17,547.30 ± 595.29
AA-BHP	1.89 ± 0.22	1.04 ± 0.68	23.20 ± 0.07	266.49 ± 10.61	17,413.58 ± 411.68
AA-CUR	1.78 ± 0.30	0.70 ± 0.31	23.38 ± 0.11	267.01 ± 10.31	17,492.10 ± 512.41
AA-HPH	1.67 ± 0.16	1.05 ± 0.56	23.27 ± 0.09	260.07 ± 10.67	17,815.54 ± 514.36
AA-AUS	1.85 ± 0.25	1.20 ± 0.64	23.45 ± 0.14	258.22 ± 10.70	18,410.21 ± 602.75
AA-ACA	1.82 ± 0.47	0.97 ± 0.25	23.28 ± 0.09	260.75 ± 10.62	17,301.00 ± 421.52
AG (apo-enzyme)	1.61 ± 0.19	1.07 ± 0.55	27.77 ± 0.06	427.02 ± 12.77	29,619.23 ± 477.95
AG-AUS	1.73 ± 0.18	0.85 ± 0.38	27.96 + 0.09	413.94 ± 13.26	30,865.47 ± 658.70
AG-GTA	2.20 ± 0.23	1.03 ± 0.57	27.83 ± 0.06	410.42 ± 12.99	30,623.51 ± 540.63
AG-VBG	1.95 ± 0.25	1.09 ± 0.63	27.76 ± 0.10	405.92 ± 13.50	29,917.13 ± 566.38
AG-MGN	1.81 ± 0.19	1.09 ± 0.56	27.99 ± 0.11	411.04 ± 15.87	30,951.06 ± 584.89
AG- HDJ	1.70 ± 0.12	1.06 ± 0.46	28.05 ± 0.09	415.38 ± 13.28	31,439.30 ± 660.19
AG-ACA	1.65 ± 0.10	1.00 ± 0.44	27.84 ± 0.08	427.01 ± 13.66	29,417.32 ± 532.42
AR (apo-enzyme)	1.59 ± 0.23	1.05 0.64±	19.33 ± 0.06	138.95 ± 8.05	13,387.83 ± 284.35
AR-HPH	1.49 ± 0.22	1.07 ± 0.66	19.17 ± 0.09	142.29 ± 8.19	12,864.95 ± 380.00
AR-BHP	1.24 ± 0.14	0.91 ± 0.51	19.11 ± 0.07	142.32 ± 7.87	12,525.95 ± 307.21
AR-AES	1.57 ± 0.21	1.09 ± 0.59	19.27 ± 0.06	140.52 ± 7.99	12,884.81 ± 275.19
AR-AUS	1.36 ± 0.14	1.03 ± 0.58	19.29 ± 0.09	134.74 ± 8.28	13,134.07 ± 315.08
AR-HDJ	1.58 ± 0.29	0.76 ± 0.32	19.18 ± 0.06	143.24 ± 8.04	12,661.33 ± 326.55
AR-EPA	2.00 ± 0.31	1.12 ± 0.73	19.45 ± 0.08	137.55 ± 7.96	13,339.97 ± 304.39
DPP-4 (apo-enzyme)	1.81 ± 0.14	1.14 ± 0.59	27.04 ± 0.10	387.26 ± 12.43	29,772.27 ± 407.99
DPP-4-HDJ	2.20 ± 0.42	1.30 ± 1.67	27.36 ± 0.21	380.75 ± 12.55	30,518.02 ± 471.31
DPP-4-CTA	1.81 ± 0.18	1.23 ± 0.70	27.12 ± 0.09	376.11 ± 14.39	30,495.52 ± 488.42
DPP-4-BHP	2.23 ± 0.33	1.30 ± 0.65	27.29 ± 0.11	387.35 ± 12.78	30,644.12 ± 571.00
DPP-4-PHA	2.12 ± 0.28	1.14 ± 0.75	27.19 ± 0.10	383.89 ± 12.19	295,88.14 ± 407.11
DPP-4-CMA	2.49 ± 0.23	1.14 ± 0.52	27.28 ± 0.12	382.29 ± 12.21	30,372.92 ± 431.08
DPP-4-SGT	2.32 ± 0.32	1.23 ± 0.84	27.23 ± 0.14	385.80 ± 12.28	29,879.51 ± 471.52
PTP1B (apo-enzyme)	1.47 ± 0.23	1.15 ± 0.54	19.37 ± 0.07	159.89 ± 8.32	13,132.84 ± 295.15
PTP1B-PHA	1.44 ± 0.20	1.13 ± 0.88	19.49 ± 0.13	156.33 ± 9.00	13,899.21 ± 563.67
PTP1B-TDA	1.39 ± 0.19	0.99 ± 0.53	19.36 ± 0.09	155.92 ± 8.78	13,415.10 ± 338.21
PTP1B-HDA	1.15 ± 0.10	1.01 ± 0.52	19.33 ± 0.06	163.00 ± 8.44	13,039.12 ± 293.12
PTP1B-MCA	1.14 ± 0.14	0.99 ± 0.54	19.25 ± 0.06	161.67 ± 8.17	13,059.97 ± 422.08
PTP1B-DCA	1.70 ± 0.28	1.14 ± 1.55	19.47 ± 0.11	155.44 ± 8.57	13,903.14 ± 284.06
PTP1B-URS	1.15 ± 0.10	1.00 ± 0.42	19.27 ± 0.06	159.76 ± 8.62	13,136.17 ± 295.29
SDH (apo-enzyme)	2.48 ± 0.44	1.35 ± 1.01	20.72 ± 0.15	131.92 ± 7.41	12,222.97 ± 332.44
SDH- ETB	2.41 ± 0.30	1.33 ± 0.99	21.16 ± 0.16	133.65 ± 7.69	12,433.06 ± 250.00
SDH-CNI	3.15 ± 0.38	1.50 ± 1.25	21.22 ± 0.19	131.58 ± 7.58	12,389.66 ± 331.358
SDH-BLD	2.42 ± 0.43	1.29 ± 0.81	21.02 ± 0.16	168.23 ± 8.86	14,797.04 ± 277.96
SDH-HDJ	2.85 ± 0.51	1.44 ± 1.00	21.21 ± 0.22	133.37 ± 7.85	12,145.93 ± 288.83
SDH-BHP	2.79 ± 0.28	1.37 ± 0.90	20.90 ± 0.12	161.22 ± 8.57	14,975.50 ± 359.245
SDH-HPS	2.91 ± 0.55	1.35 ± 0.94	21.17 ± 0.19	166.34 ± 8.38	14,759.29 ± 301.96

RMSD: root mean square deviation; RMSF: root mean square fluctuation; ROG: radius of gyration; H-bonds: hydrogen bonds; SASA; solvent accessible surface area; AA: alpha-amylase; AG: alpha-glucosidase; AR: aldose reductase; DPP-4: dipeptidyl peptidase-4; PTP1B: protein tyrosine phosphatase 1B; SDH: sorbitol dehydrogenase; AES: aesculin; BHP: (R)-7-butyl-6,8-dihydroxy-3-[(3e)-pent-3-en-1-yl]-3,4-dihydroisochromen-1-one; CUR: curvularol; HPH: (6e)-1-(4-hydroxyphenyl)-7-phenylhepta-4,6-dien-3-one; AUS: austricin; ACA: acarbose; GTA: glutaric acid; VBG: 1-O-vanilloyl-beta-D-glucose; MGN: methyl geranate; HDJ: (-)-11-hydroxy-9,10-dihydrojasmonic acid 11-beta-D-glucoside; EPA: epalrestat; CTA: caffeoyl tartaric acid; PHA: phaseic acid; CMA: p-coumaroyl malic acid; SGT: sitagliptin; TDA: tetradecanedioc acid; HDA: 2-hydroxydecanedioic acid; MCA: methylisocitric acid; DCA: dodecanedioc acid; URS: ursolic acid; ETB: erythronolide B; CNI: cnicin; BLD: blennin D; HPS: 4-[2-1R-hydroxy-ethyl)-pyrimidin-4- yl]piperazine-1-sulfonic acid dimethylamide.

Online First

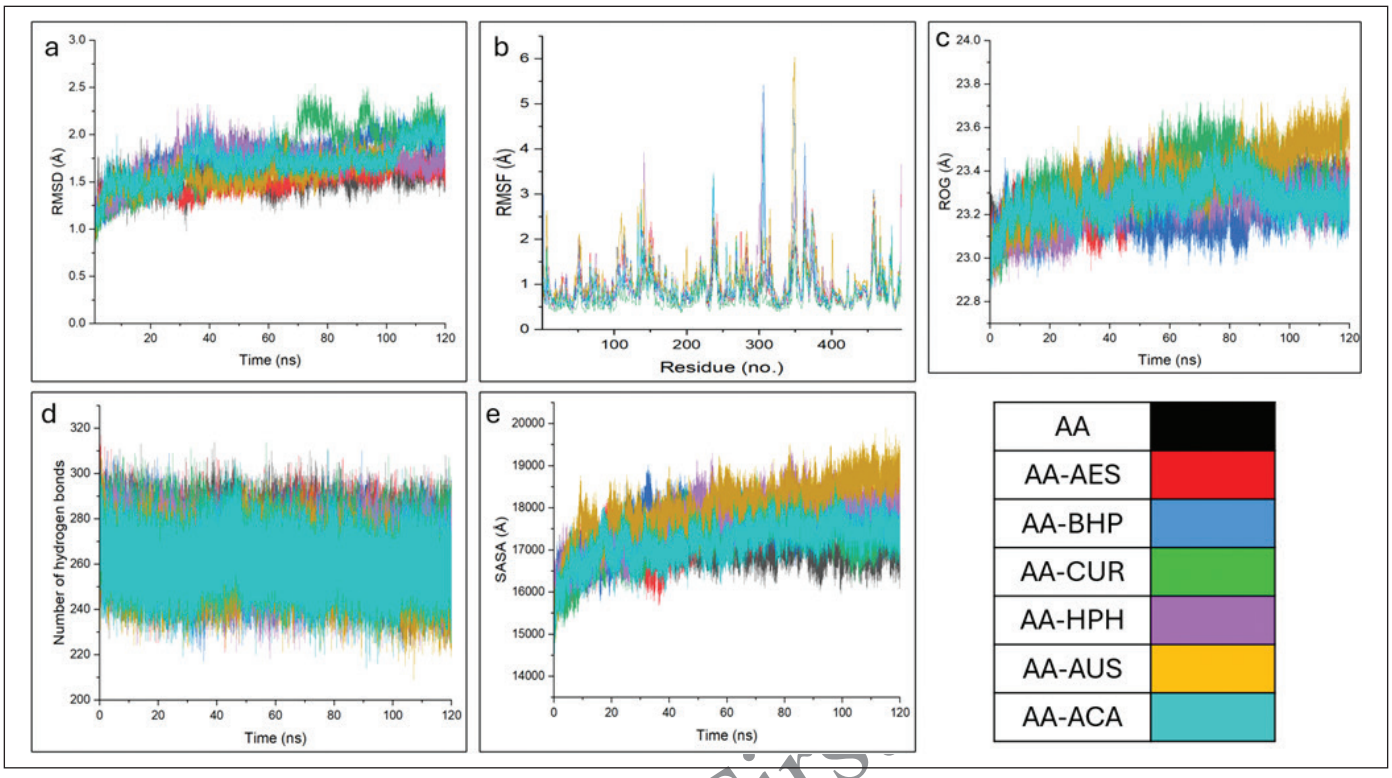

Figure 5. Post-dynamic component plots of CS metabolites-AA complexes presented as (a) RMSD, (b) RMSF, (c) ROG, (d) number of hydrogen bonds, and (e) SASA over 120 ns simulation. AA: alpha-amylase; AES: aesculin; BHP: (R)-7-butyl-6,8-dihydroxy-3-[(3e)-pent-3-en-1-yl]-3,4-dihydroisochromen-1-one; CUR: curvularol; HPH: (6e)-1-(4-hydroxyphenyl)-7-phenylhepta-4,6-dien-3-one; AUS: austricin; ACA: acarbose.

Online First

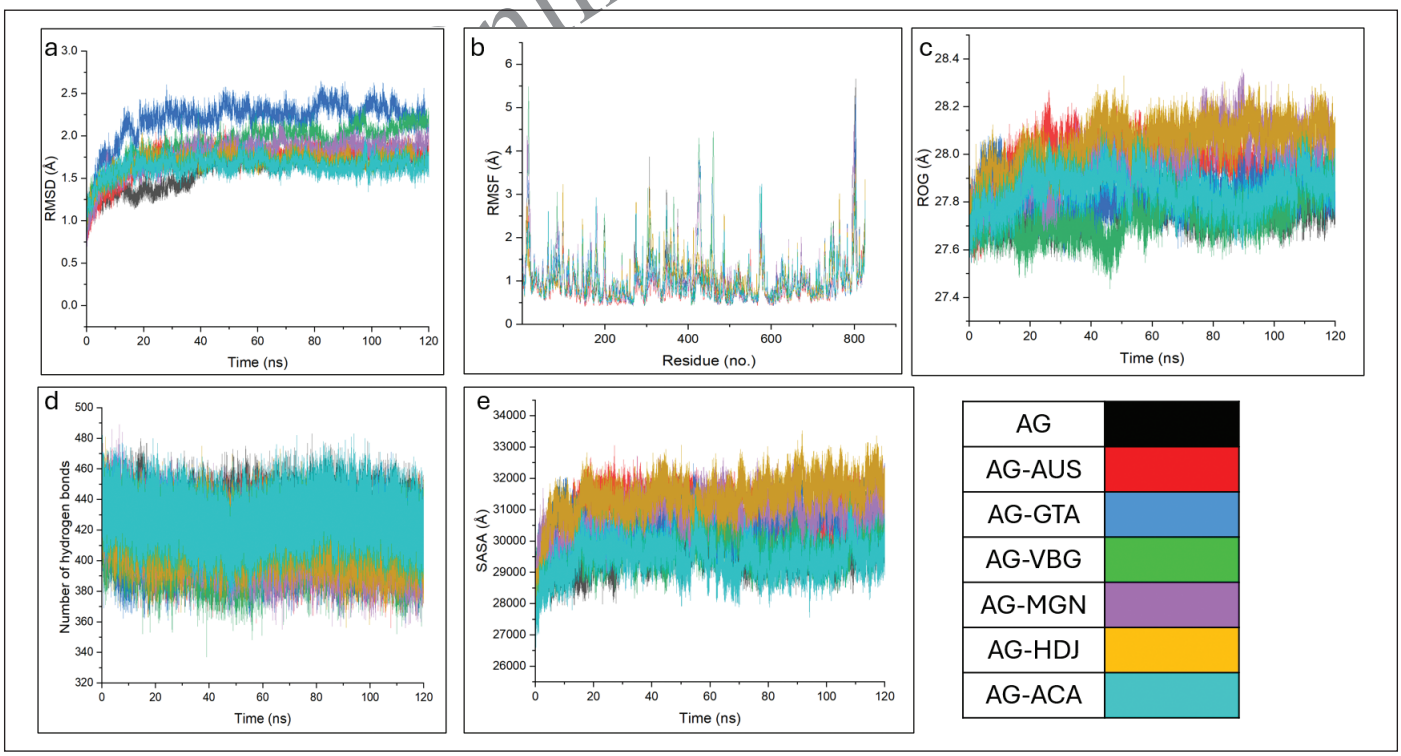

Figure 6. Post-dynamic component plots of CS metabolites-AG complexes presented as (a) RMSD, (b) RMSF, (c) ROG, (d) number of hydrogen bonds, and (e) SASA over 120 ns simulation. AG: alpha-glucosidase; AUS: austricin; GTA: glutaric acid; VBG: 1-O-vanilloyl-beta-D-glucose; MGN: methyl geranate; HDJ: (-)-11-hydroxy-9,10-dihydrojasmonic acid 11-beta-D-glucoside; ACA: acarbose.

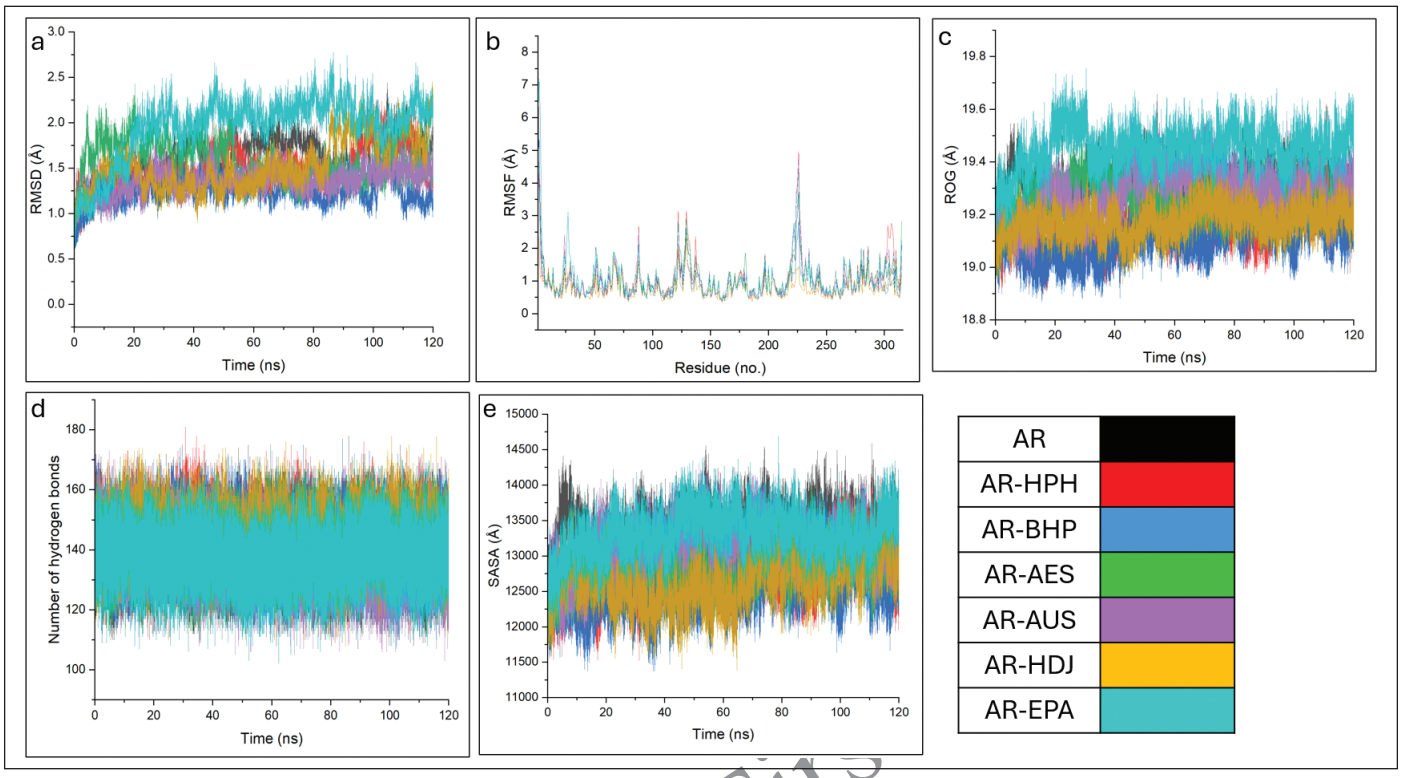

Figure 7. Post-dynamic component plots of CS metabolites-AR complexes presented as (a) RMSD, (b) RMSF, (c) ROG, (d) number of hydrogen bonds, and (e) SASA over 120 ns simulation. AR: aldose reductase; HPH: (6e)-1-(4-hydroxyphenyl)-7-phenylhepta-4,6-dien-3-one; BHP: (R)-7-butyl-6,8-dihydroxy-3-[(3e)-pent-3-en-1-yl]-3,4-dihydroisochromen-1-one; AES: aesculin; AUS: austricin; HDJ: (-)-11-hydroxy-9,10-dihydrojasmonic acid 11-beta-D-glucoside; EPA: epalrestat.

Online First

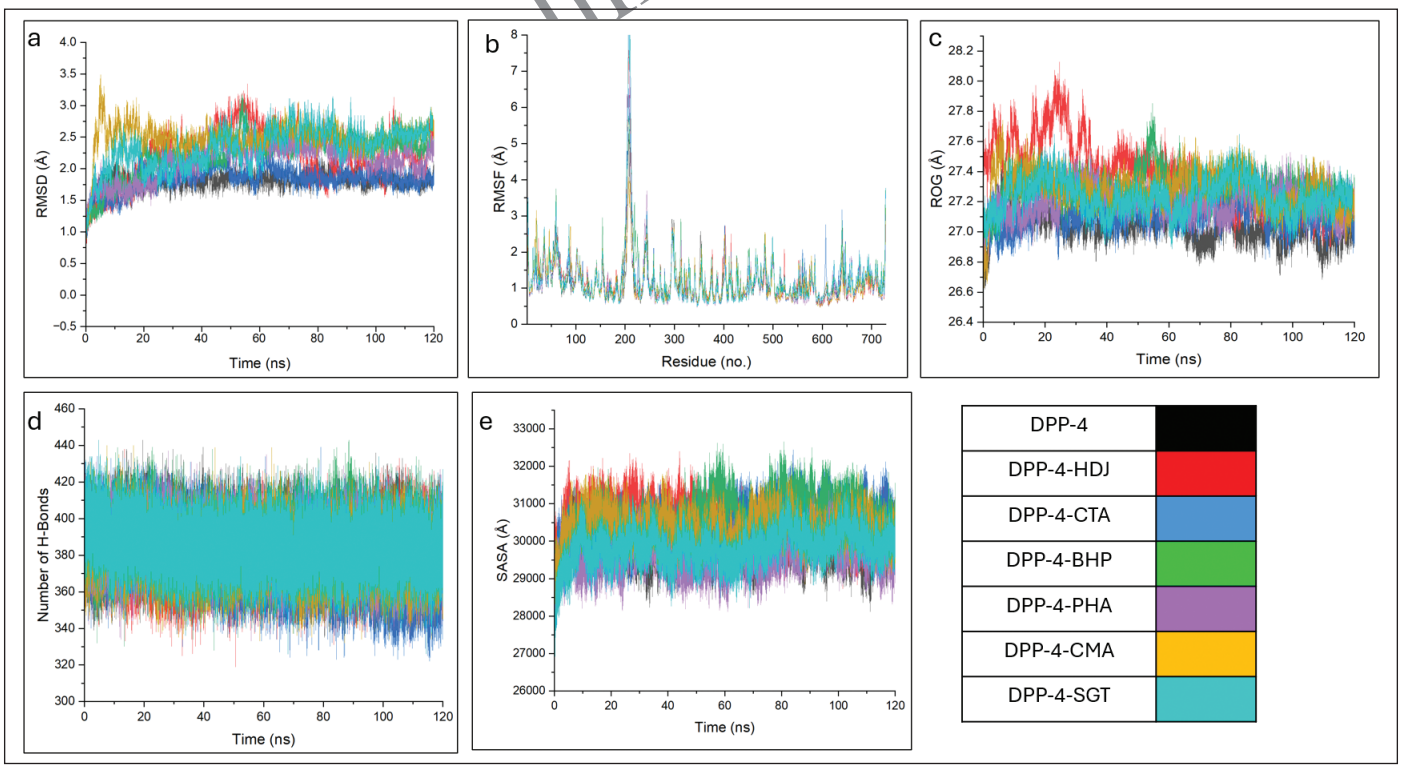

Figure 8. Post-dynamic component plots of CS metabolites-DPP-4 complexes presented as (a) RMSD, (b) RMSF, (c) ROG, (d) number of hydrogen bonds, and (e) SASA over 120 ns simulation. DPP-4: dipeptidyl peptidase-4; HDJ: (-)-11-hydroxy-9,10-dihydrojasmonic acid 11-beta-D-glucoside; CTA: caffeoyl tartaric acid; BHP: (R)-7-butyl-6,8-dihydroxy-3-[(3e)-pent-3-en-1-yl]-3,4-dihydroisochromen-1-one; PHA: phaseic acid; CMA: p-coumaroyl malic acid; SGT: sitagliptin.

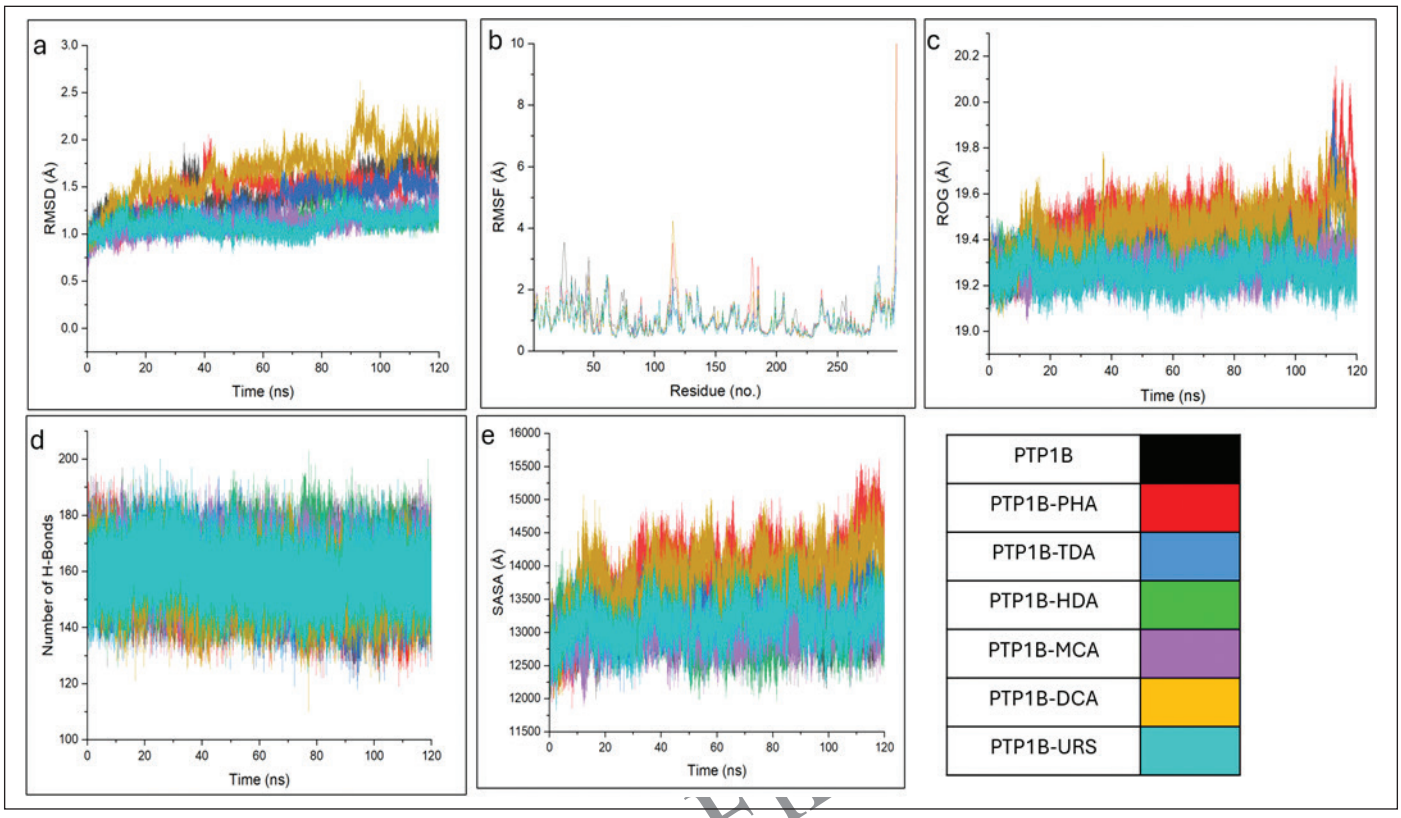

Figure 9. Post-dynamic component plots of CS metabolites-PTP1B complexes presented as (a) RMSD, (b) RMSF, (c) ROG, (d) number of hydrogen bonds, and (e) SASA over 120 ns simulation. PTP1B: protein tyrosine phosphatase 1B; PHA: phaseic acid; TDA: tetradecanedioc acid; HDA: 2-hydroxydecanedioic acid; MCA: methylisocitric acid; DCA: dodecanedioc acid; URS: ursolic acid.

Online First

AES (267.39) compared to apo-AA (266.48)]. Apart from AUS (258.22), all AA complexes exhibited a higher mean number of hydrogen bonds than ACA (260.75) (Table 3). There was a slight fluctuation between 230 and 310 in the number of hydrogen bonds formed during the 120 ns simulation period; otherwise, no major fluctuations were observed (Fig. 5d). Regarding SASA, an increase in the mean value was observed for all complexes compared to apo-AA (17130.45 Å) and ACA (17301.00 Å) (Table 3). Following a steady increase during the initial 5 ns of the simulation, all AA complexes exhibited a stable and continuous increase within the range of 16,000 Å and 19,000 Å (Fig. 5e).

3.4.2. Post-dynamic analysis of top CS metabolites against alpha-glucosidase

All AG complexes exhibited a higher average RMSD compared to both apo-AG (1.61 Å) and AG-ACA complex (1.65 Å) (Table 3). Following equilibration at 5 ns, fluctuations within the range of 0.75 Å to 2.5 Å persisted until the end of the simulation in all the bound complexes (Fig. 6a). The mean RMSF of apo-AG (1.07 Å) exceeded that of the AG-CS metabolite complexes apart from VBG (1.09 Å) and MGN (1.09 Å). Notably, the AG-AUS complex displayed the lowest average RMSF (0.85 Å) among all the complexes (Table 3). Upon binding to AG, all investigated compounds exhibited random fluctuations between 0.5 Å and 6 Å, with major fluctuations occurring sporadically across various amino acid residues (Fig. 6b). Similarly, except for VBG (27.76 Å), all AG complexes demonstrated higher mean ROG values compared to apo-AG (27.77 Å) (Table 3). The ROG of all AG complexes fluctuated between 27.5 Å and 28.2 Å, with a decrease in ROG plot for the VBG complex observed between 40 ns and 50 ns, as shown in Figure 6c. In contrast to apo-AG (427.02), a reduction in the mean number of hydrogen bonds was observed for all AG complexes (Table 3). Throughout the 120 ns simulation, the number of hydrogen bonds formed between AG complexes ranged from 360 to 470, showing no significant fluctuations in the plot (Fig. 6d). However, higher average SASA values were observed for all AG complexes relative to apo-AG (29619.23 Å) and AG-ACA (29417.32 Å) (Table 3). After an equilibration in the SASA plot at 10 ns and 27,000 Å, all AG complexes fluctuated between 28,000 Å and 32,500 Å till the end of the simulation (Fig. 6e).

3.4.3. Post-dynamic analysis of top CS metabolites against aldose reductase

A decrease in the mean RMSD was noted for all AR complexes compared to the apo-AR (1.59 Å), except for EPA (2.00 Å), which exhibited an increase in the mean RMSD (Table 3). Following a steady rise in RMSD from 0.5 Å during the initial 5 ns of the simulation, the system reached equilibrium, and the RMSD of all AR complexes varied between 0.9 Å and 2.5 Å (Fig. 7a). All examined AR complexes displayed a decline in the average RMSF, with HDJ exhibiting the lowest mean RMSF (0.76 Å) compared to apo-AR (1.05) and AR-EPA (1.12) (Table 3). After an initial decrease in RMSF during the first 5 ns of the simulation, all AR complexes fluctuated between 0.5

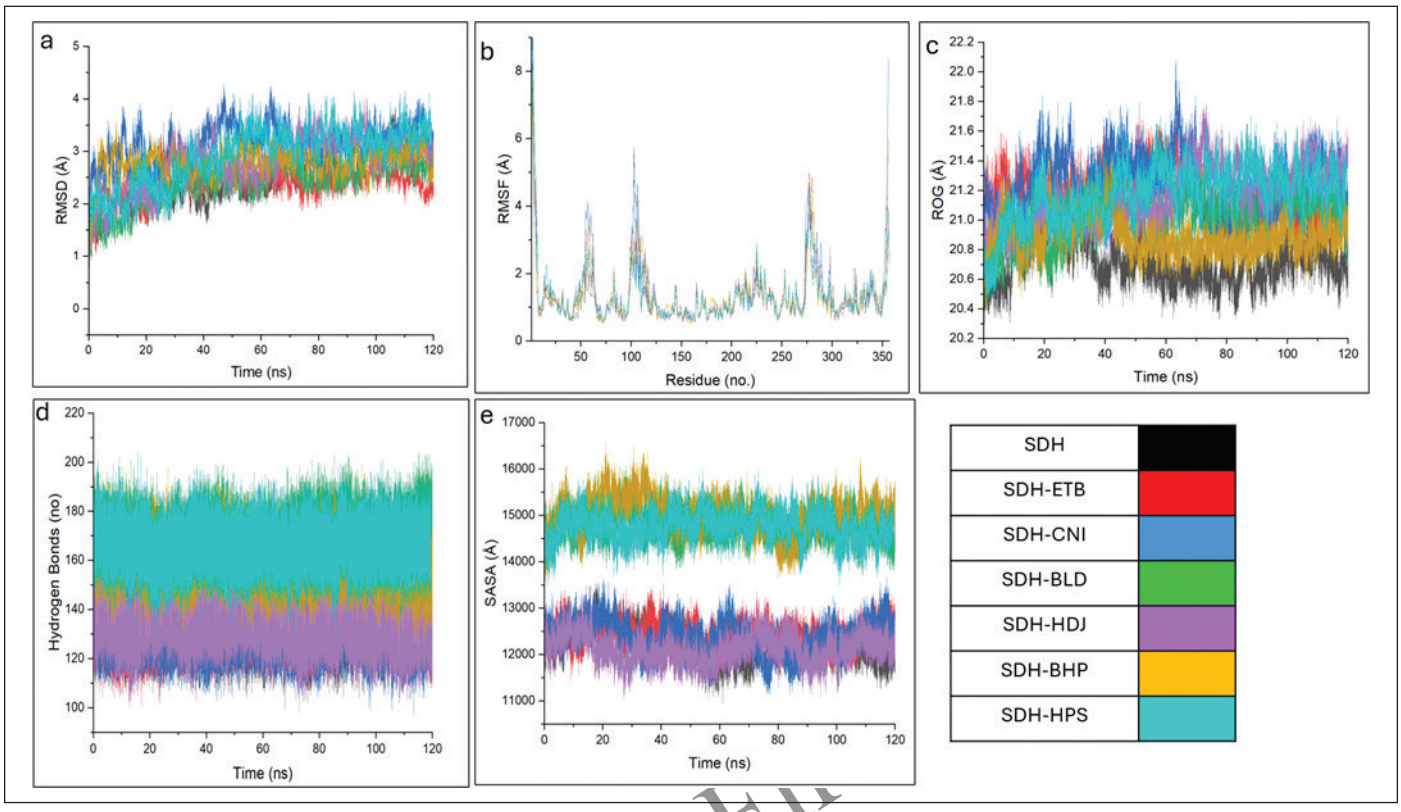

Figure 10. Post-dynamic component plots of CS metabolites-SDH complexes presented as (a) RMSD, (b) RMSF, (c) ROG, (d) number of hydrogen bonds, and (e) SASA over 120 ns simulation. SDH: sorbitol dehydrogenase; CNI: cnicin; BLD: blennin D; HDJ: (-)-11-hydroxy-9,10-dihydrojasmonic acid 11-beta-D-glucoside; BHP: (R)-7-butyl-6,8-dihydroxy-3-[(3e)-pent-3-en-1-yl]-3,4-dihydroisochromen-1-one; HPS: 4-[2-1R-hydroxy-ethyl)-pyrimidin-4- yl]piperazine-1-sulfonic acid dimethylamide.

Online Fi

Å and 5 Å, with notable fluctuations observed in residues 25–50, 50–60, 75–90, 130–150, and 215–250 (Fig. 7b). Similarly, all AR complexes demonstrated a decrease in their average ROG values compared to apo-AR (19.33), except for EPA, which presented an average ROG value of 19.45 Å (Table 3). Throughout the simulation, the ROG fluctuated between 19.8 Å and 19.75 Å, with higher variations observed in EPA and AR-HDJ (Fig. 7c). All AR complexes displayed a higher number of hydrogen bonds compared to apo-AR (138.95), except for AUS (134.74) (Table 3). The number of hydrogen bonds for all AR complexes ranged from 110 to 170, with no major fluctuations observed (Fig. 7d). In contrast to apo-AR (13387.83 Å), all AR complexes exhibited a decrease in mean SASA values, except for EPA (13339.97 Å) (Table 3). Following an initial increase in SASA during the first 5 ns, all AR complexes fluctuated between 11,500 Å and 14,500 Å, without significant variations (Fig. 7e).

3.4.4. Post-dynamic analysis of top CS metabolites against DPP-4

All DPP-4 complexes exhibited higher average RMSD values relative to the apo-DPP-4 (1.81 Å) except for CTA (1.81 Å), which was similar to apo-DPP-4 (Table 3). After an initial increase in RMSD from 0.5 Å, all DPP-4 complexes fluctuated between 1.25 Å and 3.5 Å with CMA and HDJ showing major fluctuations at 8 ns and 50 ns, respectively (Fig. 8a). In contrast to apo-DPP-4 (1.14 Å), all DPP-4 complexes had higher mean RMSF, except PHA (1.14 Å) and CMA (1.14 Å) with equal average RMSF value (Table 3). The RMSF of all DPP-4 complexes fluctuated between 0.5 and 3.5 Å, except for a major fluctuation increase to 8 Å between residues 200 and 240 (Fig. 8b). All DPP-4 complexes showed an increase in mean ROG in comparison to apo-DPP-4 (27.04 Å) (Table 3). After an increase in ROG from 26.6 Å during the first 5 ns, all DPP-4 complexes fluctuated between 26.8 Å and 27.3 Å except for HDJ and BHP, which had increases ranging between 27.8 and 28.1 Å between 20 ns to 40 ns and 50 ns to 60 ns, respectively (Fig. 8c). All DPP-4 complexes showed a reduction in the mean number of hydrogen bonds in comparison to apo-DPP-4 (387.26), except for the BHP complex (387.35) (Table 3). The number of hydrogen bonds fluctuated between 320 and 440 throughout the 120 ns simulation (Fig. 8d). Relative to apo-DPP-4 (29772.27 Å), all DPP-4 complexes showed an increase in mean SASA except for PHA (29588.14 Å) (Table 3). Once the complexes equilibrated after 10 ns, the SASA of all DPP-4 complexes fluctuated between 28,500 and 32,500 Å (Fig. 8e).

3.4.5. Post-dynamic analysis of top CS metabolites against PTP1B

When bound to PTP1B, all compounds exhibited a reduction in mean RMSD in comparison to apo-PTP1B (1.47 Å), except for DCA (1.70 Å). Notably, MCA displayed the lowest mean RMSD of 1.14 Å when bound to PTP1B, lower than the PTP2B-URS complex (1.15 Å) (Table 3). Following an initial increase during the first 10 ns of the simulation, all PTP1B complexes exhibited fluctuations within the range of 0.75–2.00 Å, except for DCA, which fluctuated to 2.5 Å between 85 ns and 105 ns (Fig. 9a). In comparison to the apo-

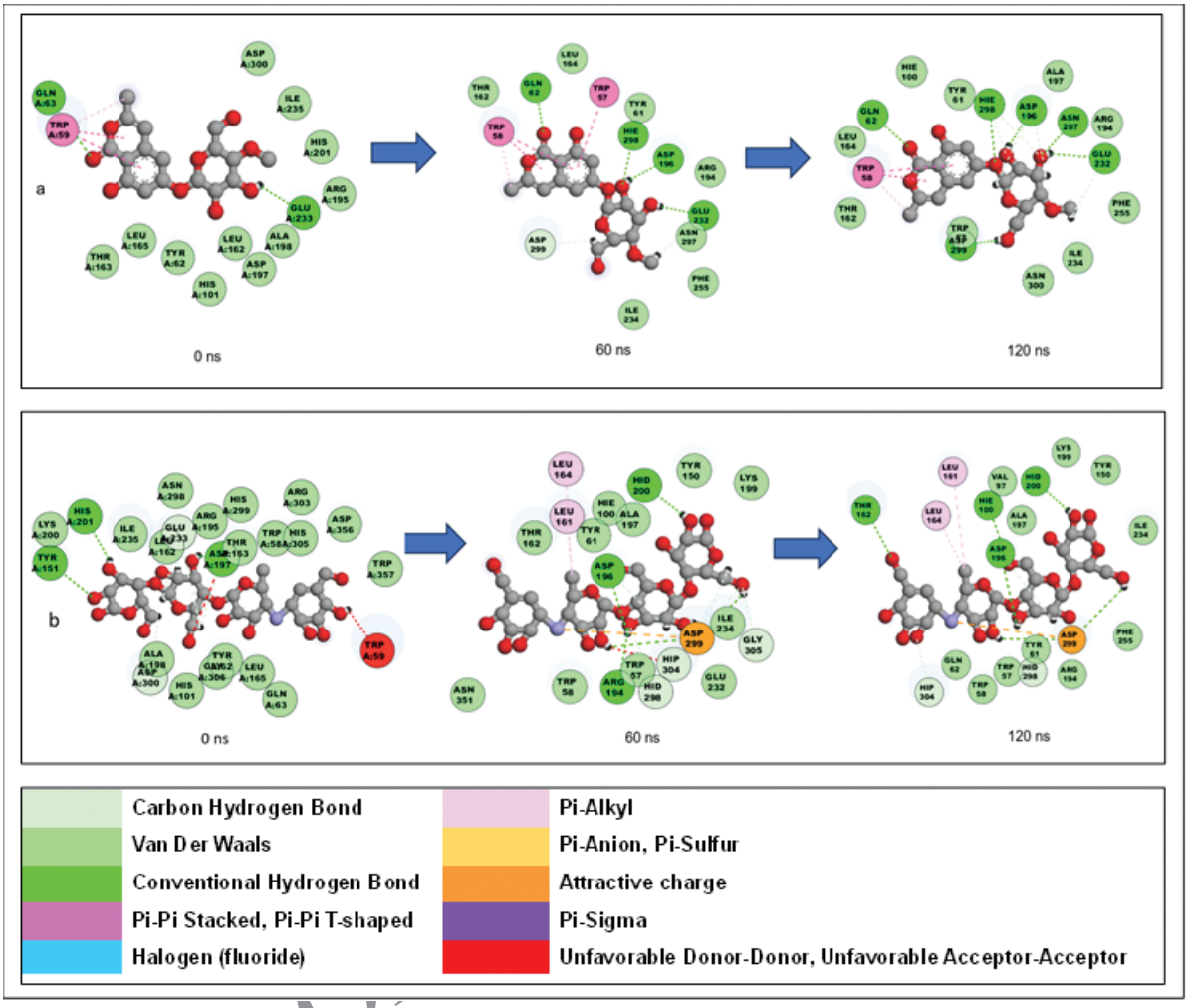

Figure 11. 2-D interaction plots following the binding of AA to (a) (R)-7-butyl-6,8-dihydroxy-3-[(3e)-pent-3-en-1-yl]-3,4-dihydroisochromen-1-one and (b) acarbose over 120 ns simulation.

PTP1B (1.15 Å), all PTP1B complexes had lower RMSF values, with MCA and TDA exhibiting the lowest mean RMSF of 0.99 ÅÅ, both notably comparable to URS (1.00 Å) (Table 3). The RMSF for all complexes varied within the range of 0.5 Å to 4.00 Å. Notably, DCA, TDA, and PHA displayed an increase in RMSF, ranging from 5.80 Å to 9.80 Å, specifically at residues 280–299 (Fig. 9b). The mean ROG of all PTP1B complexes was comparably lower than apo-PTP1B (19.37 Å), with the exception of PHA (19.49 Å) and DCA (19.47 Å). Interestingly, MCA (19.25 Å) exhibited the lowest mean RMSF, which was marginally less than URS (19.27 Å) (Table 3). During the 120 ns simulation, the ROG of all PTP1B complexes fluctuated between 19.05 Å to 19.75 Å, except DCA, TDA, and PHA, with terminal fluctuations ranging from 19.90 Å to 20.10 Å between 110 and 120 ns (Fig. 9c). The average number of hydrogen bonds formed between the PTP1B complexes compared to apo-PTP1B (159.89) decreased during the simulation, with the exception of MCA (161.67) and HDA (163.67), which were comparably higher (Table 3). The number of hydrogen bonds formed between all the PTP1B complexes ranged between 120 and 190 during the 120 ns simulation (Fig. 9d). All PTP1B complexes revealed a higher average SASA in contrast to apo-PTP1B (13132.84 Å), except for HDA (13039.12 Å) and MCA (13059.97 Å), which were notably lower (Table 3). After an increase in the SASA values during the initial 5 ns, all PTP1B complexes fluctuated between 12,250 and 145,000 Å with PHA and DCA increasing to 15,250 Å at the end of the simulation (Fig. 9e).

3.4.6. Post-dynamic analysis of top CS metabolites against SDH

When bound to SDH, the investigated compounds displayed elevated mean RMSD values than apo-SDH (2.48 Å), with the exception of ETB (2.41 Å) and BLD (2.45 Å), both of which exhibited lower values. In comparison to the AA-HPS (2.91 Å) (standard) complex, all SDH-CS complexes had lower mean RMSD, except for CNI (3.15 Å) (Table 3). The examined SDH complexes had RMSD values ranging from 1.00 Å to 4.00 Å during the simulation (Fig. 10a). The mean RMSF of apo-SDH (1.35 Å) complex and SDH-HPS (1.35 Å) complex were lower in comparison to the SDH-CS metabolite complexes, except for ETB (1.33 Å) and BLD (1.29 Å). Following a decline in the range of residues 0–10, the RMSF of the scrutinized SDH complexes exhibited fluctuations spanning from 0.50 Å to 3.00 Å until residue 350. Pronounced

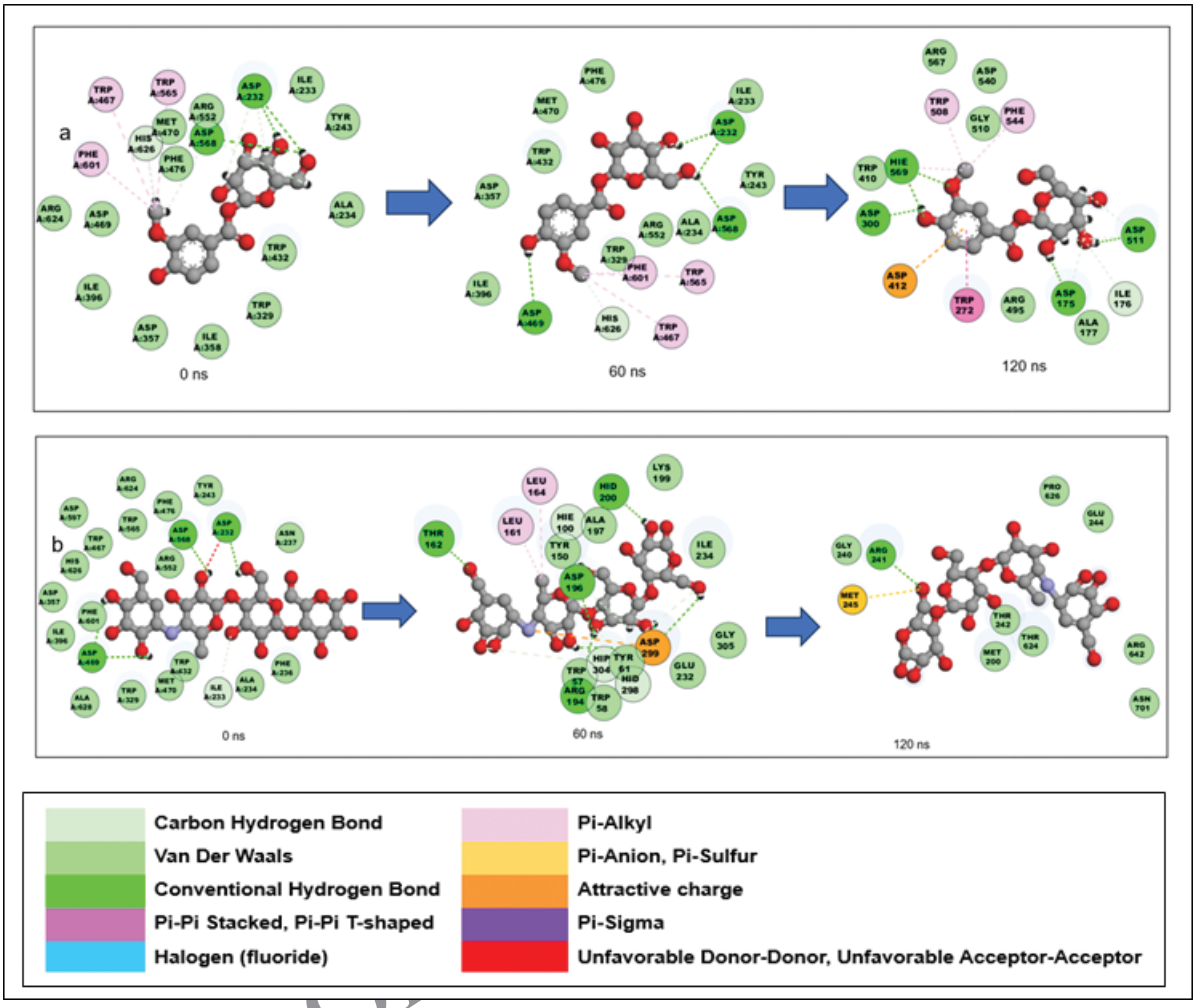

Figure 12. 2-D interaction plots following the binding of alpha-glucosidase to (a) 1-O-vanilloyl-beta-D-glucose and (b) acarbose over 120 ns simulation.

variations were noted particularly between residues 40–75, 100–125, and 260–300, culminating in a significant upsurge in RMSF to 8.30 Å observed around residues 350–356 (Fig. 10b). In comparison to apo-SDH (20.72 Å), the investigated SDH complexes demonstrated higher mean ROG values. However, CS metabolites BHP (20.90 Å) and BLD (21.02 Å) had lower mean ROG when bound to SDH in comparison to the standard HPS (21.17 Å) (Table 3). Throughout the 120 ns simulation, fluctuations in ROG were observed, with the complexes showcasing a range between 20.30 Å and 22.10 Å (Fig. 10c). Regarding the mean number of hydrogen bonds formed among the SDH complexes, all displayed an increase compared to apo-SDH (131.92), except CNI (131.58), which demonstrated a relatively similar number of hydrogen bonds. Interestingly, BLD (168.23) exhibited a higher number of hydrogen bonds in comparison to HPS (166.34) (Table 3). Throughout the 120 ns simulation, the number of hydrogen bonds exhibited fluctuations ranging between 100 and 200 for the SDH complexes. Notably, HPS and BLD stood out by displaying a higher number of hydrogen bonds when bound to SDH (Fig. 10d). Among the SDH complexes, several displayed an increase in the mean SASA when compared to apo-SDH (12222.97 Å), except for HDJ (12145.93 Å), which had the lowest mean SASA value (Table 3). The SASA of all SDH complexes varied from 11,250 to 16,500 Å, with the larger values attributed to BHP and HPS (Fig. 10e).

3.4.7. 2D interaction plot analysis of top CS metabolites against the investigated diabetes enzymes

The 2D interaction plots of the top-ranked CS compounds (highest negative ΔG_{bind}) against their respective target enzymes over the 120 ns simulation showed various types of bonds, namely hydrogen bonds (conventional and carbon), attractive charge, Van der Waals, pi-pi-stacked, pi-pi T-shaped, pi-cation, pi-anion, pi-alkyl, alky, halogen (fluoride), and unfavorable acceptor–acceptor and donor–donor interactions (Fig.s 11–16). While AA and BHP formed 19 interactions, AA and ACA formed 22 interactions (Fig. 11) at 120 ns. AG and VBG had 19 interactions, but with ACA, only 10 interactions were observed (Fig. 12). For aldose reductase, HDJ formed 22 interactions while EPA formed 20 interactions, including (Fig. 13). CMA binds to DPP-4 with 13 interactions, while SGT binds with 16 interactions (Fig. 14). The binding of HDA, URS to PTP1B resulted in 11 and

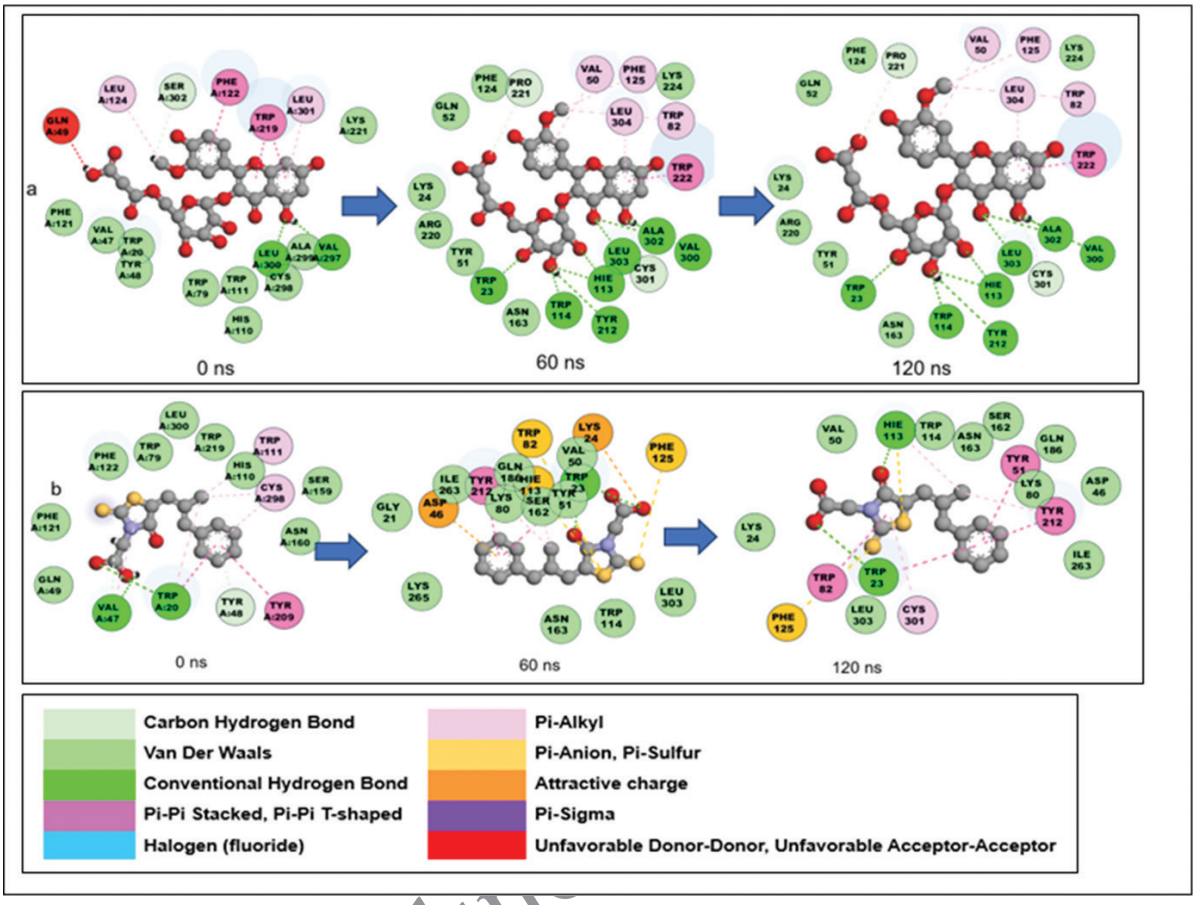

Figure 13. 2-D interaction plots following the binding of AR to (a) (-)-11-hydroxy-9,10-dihydrojasmonic acid 11-beta-D-glucoside and (b) epalrestat over 120 ns simulation.

Online

12 interactions, respectively (Fig. 15). Finally, the SDH-HDJ complex showed 22 interactions, while HPS showed 9 (Fig. 16). The details of the interacting residues categorized as hydrogen and hydrophobic interactions post 120 ns simulation are summarized in Table 4.

3.5. Frontier molecular orbitals of the top-ranked compounds

The top-ranked compounds and reference standards had LUMO energies ranging between −5.92 and −0.22 eV, except ACA (−0.89 eV) and URS (−0.24 eV). However, the HOMO energies of the standards fall within the same range as the top compounds (−5.85 and −7.72 eV) (Table 5 and Fig. 17). The lowest energy gap among the top-ranked compounds was observed in HPH (3.61 eV), AUS (4.70 eV), HPH (3.61 eV), CTA (4.06 eV), PHA (4.41 eV), and CNI (4.46 eV) against AA, AG, AR, DPP-4, PTPIB, and SDH, respectively; however, a lower energy gap was observed in the two reference standards; EPA (3.21 eV) and HPS (4.39 eV) against AR and SDH, respectively (Table 5 and Fig. 17). Consequently, these compounds exhibited varying softness and lowest hardness values, respectively [HPH (0.55 and 1.80 eV), AUS (0.43 and 2.35 eV), HPH (0.55 and 1.80 eV), CTA (0.50 and 2.03 eV), PHA (0.45 and 2.20 eV), and CNI (0.45 and 2.23 eV)]. Notably, PHA had the highest ionization energy (2.30 eV), electronegativity (4.50 eV), electrophilicity index (4.59 eV), and the lowest chemical potential (−4.50 eV), while GTA had the highest electron affinity (7.72 eV) Table 5 and Supplementary Table S5. Summarily, the cDFT parameters of the top-ranked compounds taken for MD simulation and the reference standards are presented in Table 5, while those of DCA, TDA, MCA, and PHA have been previously reported [41].

3.6. Toxicity prediction of the top-ranked compounds

To gain insights into the safety of the top-ranked compounds following MD simulation, the compounds were subjected to ProTox toxicity prediction. The emerging top compounds against the diabetes targets had a minimum lethal dose (LD_{50}) of > 400 mg/kg and toxicity class > 3, except for curvularol, austricin, and methyl isocitric acid, which presented < 200 mg/kg LD_{50} and toxicity class ≤ 3 (Table 6). All the compounds showed no hepatotoxicity potential and were mostly nonend-point toxicants (Table 6). The other four top compounds for each target equally demonstrated relatively high tolerable doses, no organ and end-point toxicities, and compared well with the available standard drugs.

4. DISCUSSION

Humanity has relied on nature to provide food, shelter, clothing, transportation, fertilizers, flavors and fragrances, and

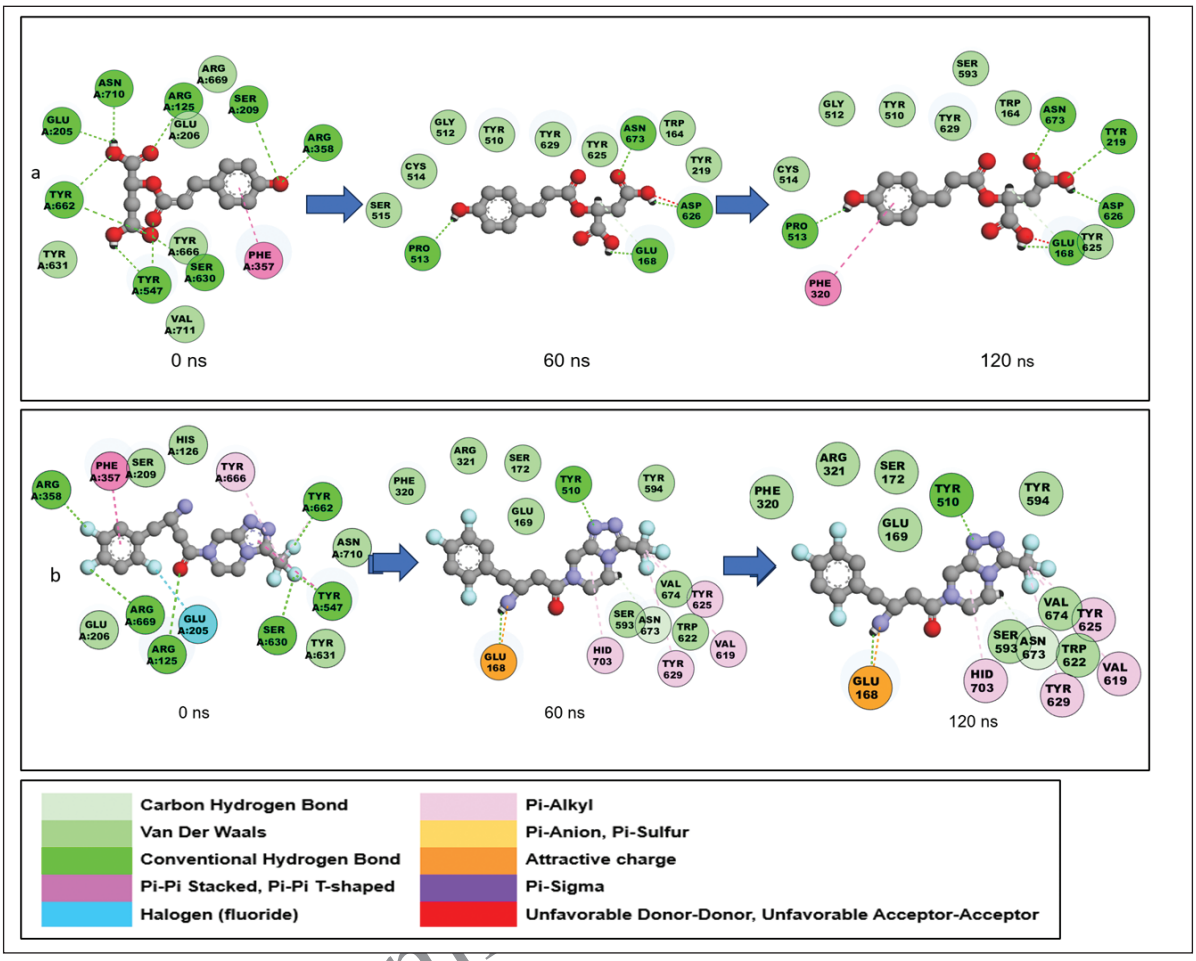

Figure 14. 2-D interaction plots following the binding of DPP-4 to (a) p-coumaroyl malic acid and (b) sitagliptin over 120 ns simulation.

notably, medicinal resources among others [57]. For centuries, plants with medicinal attributes have formed the basis of the traditional systems of medicine [24], which have been continuously developed to provide new remedies to treat and/or manage several diseases and illnesses [57], including T2DM [58]. For instance, despite being a waste material of corn, CS has been identified as a possible therapeutic agent for T2DM management [27], and several other biological properties such as diuretic, antihyperlipidemic, antihypertensive, anti-obesity, anti-microbial, neuroprotective, anti-cancer, anti-depressant, antioxidant, anti-inflammatory, and antidiabetic [29,31,32].

Amongst several factors that influence the phytochemical profile of therapeutically significant plants and plant materials (such as CS), determining the changes in chemical and bioactive components throughout the maturation process is crucial for identifying the optimal harvest time that ensures the highest level of therapeutic activity [59]. The high concentration of metabolites profiled at the mature stage of CS relative to the premature stage suggests accumulation of the secondary metabolites during the maturation process of CS [60]. The observed variation in life or developmental cycle of a plant may be likened to the report of Sarepoua *et al*. [61], wherein, despite the presence of certain metabolites in abundance during the silking phase (premature), the milking stage (mature) exhibited the highest levels of secondary metabolites such as total phenolic content, total flavonoid content, total anthocyanin content and antioxidant capacity. Similarly, Abeywardhana *et al*. [62] demonstrated that the therapeutic potential of *Ocimum sanctum* is more pronounced at the fully matured stage compared to the premature stage. The increase in therapeutic potential at more mature phases of a plant or plant material may be attributed to a higher presence of therapeutic compounds [26].

Aside from the influence of the developmental (mature) stage contributing to the abundance of secondary metabolites, the processing conditions may also influence the composition and quantity of metabolites within CS [32]. In fact, the elevated abundance of various compounds in the raw CS samples suggest that the processing of CS during extract preparation (such as drying, grinding, boiling, and alcoholic solvent extraction) had an impact on the quantity of these metabolites in the processed CS samples [63]. In traditional systems of medicine, the simplest and most popular methods for preserving the medicinal properties of CS involve aqueous, hydro-ethanolic, and ethanolic extractions [64,65], since the type of solvent used for extraction plays a role in the types and amounts of phytoconstituents extracted [28,66].

Metabolites identified in CS extracts, such as 1-O-vanilloyl-beta-D-glucose, a hydrolysable tannin with potential antidiabetic properties [67], have their variant,

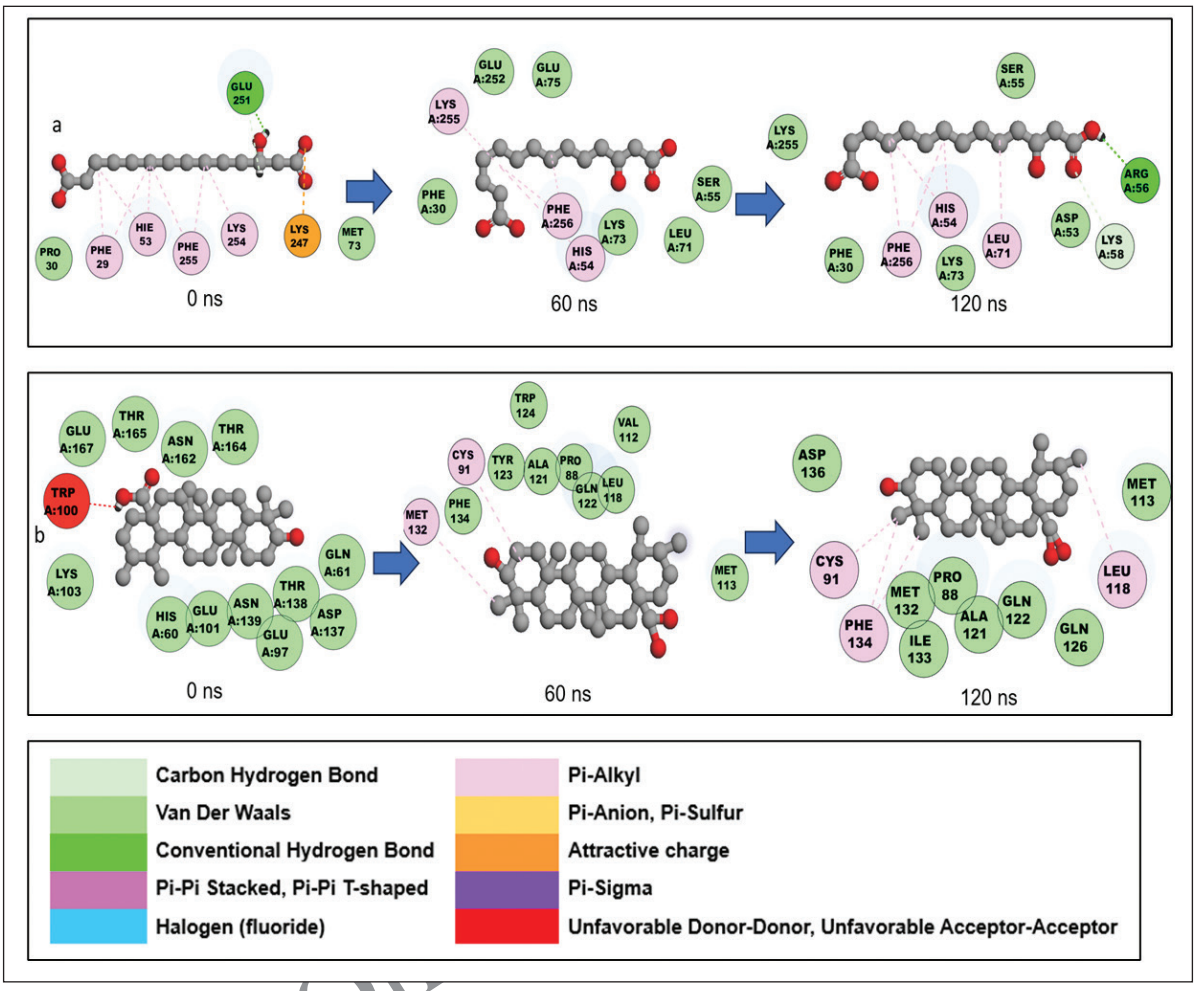

Figure 15. 2-D interaction plots of PTP1B bound to (a) CS metabolite 2-hydroxydecanedioic acid and (b) ursolic acid over 120 ns simulation.

6-O-vanilloyl-beta-D-glucose being reported to inhibit a-amylase activity [68]. (R)-7-butyl-6,8-dihydroxy-3-[(3e)-pent-3-en-1-yl]-3,4-dihydroisochromen-1-one is a derivative of 3,4-dihydroisocoumarin with antidiabetic activity [69]. Similarly, (-)-11-hydroxy-9,10-dihydrojasmonic acid 11-beta-D-glucoside and (-)-11-hydroxy-9,10-dihydrojasmonic acid 11-beta-D-glucoside are glucoside derivatives of (-)-11-hydroxy-9,10-dihydrojasmonic acid identified in *Gymnema sylvestre* and *Combretum micranthum* and presented significant binding interaction with α-amylase, α-glucosidase, and phosphorylated insulin receptor tyrosine kinase to elicit an antidiabetic effect [70]. P-coumaroyl malic acid, a derivative of p-coumaric acid, is formed from the esterification of the carboxy group of p-coumaric acid with the hydroxyl group of malic acid. P-coumaric acid has been noted for attenuating elevated blood glucose [71]. Hydroxydecanedioic acids and their derivatives are water-soluble salts been implicated in T2DM treatment [72]. A proposed pathway for the biosynthesis of some of the metabolites identified in CS is depicted in Supplementary Figure 8. Among the CS samples, the hydro-ethanolic extract of mature CS displayed a higher abundance of most metabolites. The higher concentration of metabolites in the hydro-ethanolic extract of mature CS is attributed to the moderate polarity of hydro-ethanol, suggesting that the majority of the metabolites in CS are moderately polar [28,66,73]. Furthermore, Lipinski's Ro5 was mostly considered due to its simplicity and practicability in selecting metabolites of remarkable oral pharmacokinetics profiles for drug development purposes was employed in this study to screen the metabolites for subsequent computational studies.

Molecular docking accessed the CS metabolites' docking scores at active sites of the investigated enzymes, with higher negative scores indicating stronger ligand attraction [72–74]. The more negative docking scores of AES, AUS, HPH, HDJ, PHA, and ETB compared to the reference standards against AA, AG, AR, DPP-4, PTP1B, and SDH, respectively, indicate their better binding affinities, interaction, superiority, and their greater suitability or fitness as possible therapeutics [75–79]. Although there are no studies that have previously explored the top-ranked CS metabolites relative to the investigated enzyme targets, Chaudhary *et al*. [80] revealed that CS compounds gallotannin, 3-O-caffeoylquinic acid, stigmasterol and formononetin (7-hydroxy-4'-methoxyisoflavone) had higher negative docking scores against DPP-4 (−10.7 kcal.mol), AG (−8.9 kcal.mol), AA (−9.8 kcal.mol), and PTP1B (−8.7 kcal.mol), highlighting the ability of CS metabolites to modulate

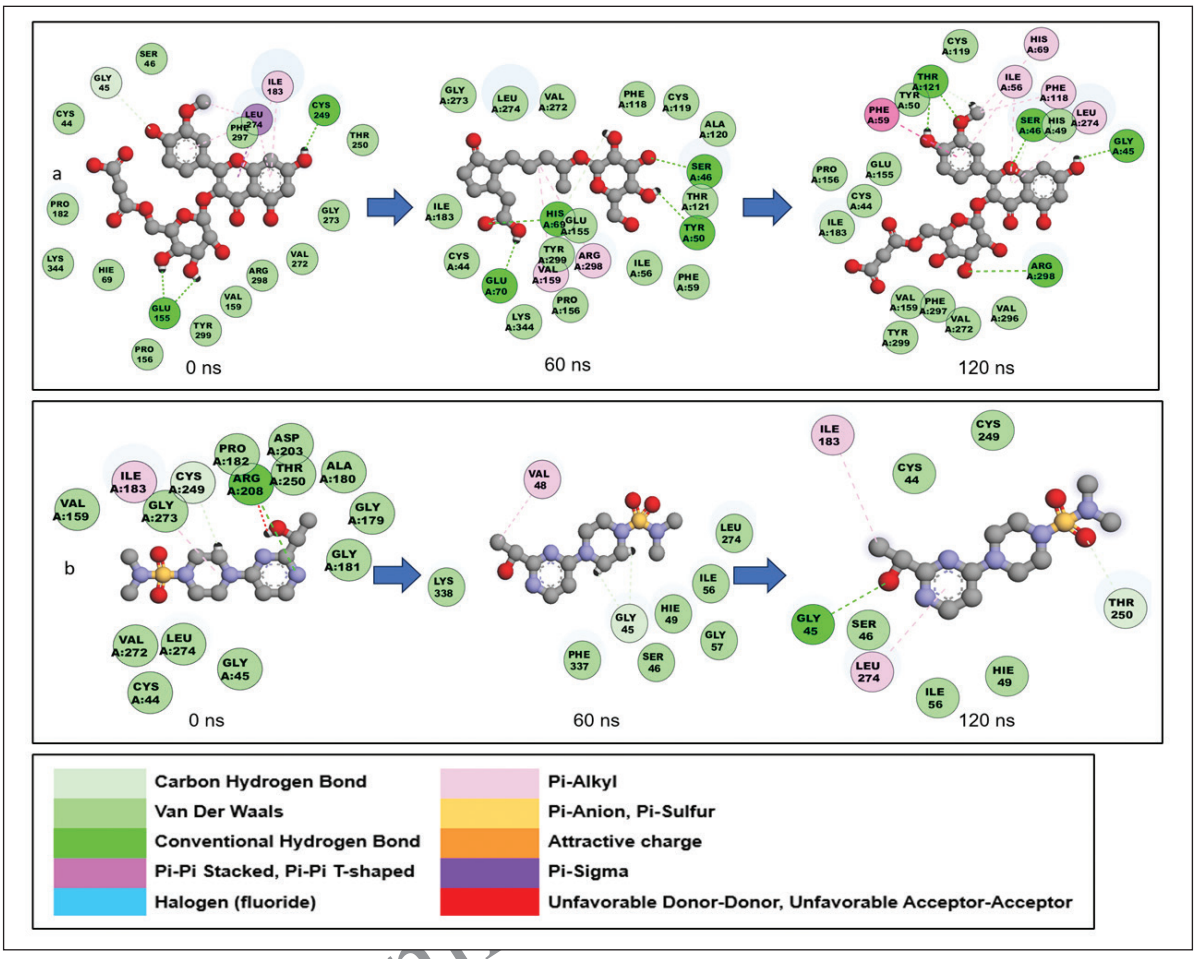

Figure 16. 2-D interaction plots of SDH bound to (a) (-)-11-hydroxy-9,10-dihydrojasmonic acid 11-beta-D-glucoside and (b) 4-[2-1R-hydroxy-ethyl)-pyrimidin-4-yl] piperazine-1-sulfonic acid dimethylamide over 120 ns simulation.

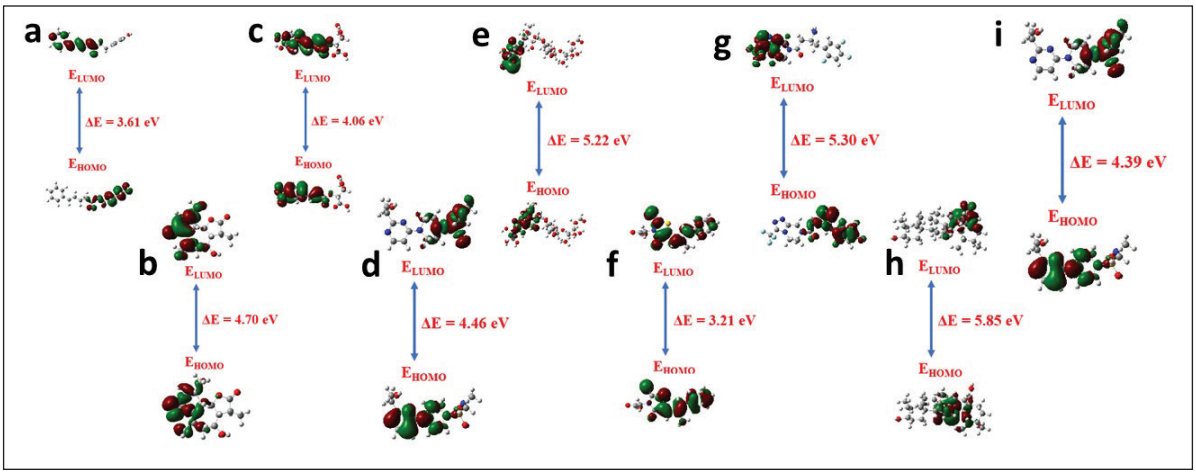

Figure 17. Frontier molecular orbitals for (a) hydroxyphenyl)-7-phenylhepta-4,6-dien-3-one (HPH), (b) austricin (AUS), (c) caffeoyl tartaric acid (CTA), (d) cnicin (CNI), (e) acarbose (ACA), (f) epalrestat (EPA), (g) sitagliptin (STG), (h) ursolic acid (URS), and (i) 4-[2-1R-hydroxy-ethyl)-pyrimidin-4- yl]piperazine-1-sulfonic acid dimethylamide (HPS)

the activity of key enzymes implicated in the pathogenesis of T2DM. Similarly, Sabiu *et al*. [8] demonstrated that phenolic compounds from *Carpobrotus edulis*, such as chlorogenic acid, luteolin-7-O-glucoside, epicatechin, and isorhamnetin-3-O-rutinoside had commendable binding at the active site of AA, AG, and AR.

Table 4. Bond interaction analysis of the targets of top 5 identified metabolites of corn silk against the target enzymes.

Complexes	Total interactions	Hydrogen bond interactions	Hydrophobic interactions
			AA
BHP	19	6 [GLN 62, ASP 196, GLU 232, ASN 297, HIE 298 and ASP 299]	10 [Van der Waals (TRP 57, TYR 61, HIE 100, THR 162, LEU 164, ARG 195, ALA 197, ILE 234, PHE 255, and ASN 300), 1 pi-pi stacked (TRP 58) 1 pi-pi T-shaped (TRP 58) and 1 pi-alkyl (TRP 58]
ACA	22	8 [HIE 100, THR 163, ASP 196, HID 200, HID 298, 2 at ASP 299, and HIP 300]	11 [Van der Waals (TRP 57, TRP 58, TYR 61, GLN 62, VAL 97, TYR 150, ARG 194, ALA 197, LYS 199, ILE 234, and PHE 255), 2 pi-pi alkyl (LEU 161 and LEU 162) and 1 pi-anion (ASP 299)]
			AG
VBG	19	8 [2 (ASP 175), ILE 176, 2 (HIE 569), ASP 300 and 2 (ASP 511)]	6 [Van der Waals (ALA 177, TRP 410, ARG 495, GLY 510, ASP 540, and ARG 567), 1 pi-anion (ASP 412), 1 pi-pi stacked (TRP 272) and 3 pi-alkyl (TRP 508, PHE 544, and HIE 569)]
ACA	10	1 [ARG 241]	8 [Van der Waals (MET 200, GLY 240, THR 242, GLU 244, PRO 626, THR 642, ARG 642, and ASN 701) and 1 pi-anion (MET 245)]
			AR
HDJ	22	10 [TRP 23, 2 at HIE 113, TRP 114, TYR 219, PRO 221, VAL 300, CYS 301, ALA 302, and LEU 303]	7 [Van der Waals (LYS 24, TYR 51, ASN 163, ARG 220, GLN 52, PHE 124 and LYS 224), 4 pi-alkyl (VAL 50, TRP 80, PHE 125 and LEU 304), 1 pi-pi stacked (TRP 222)]
EPA	20	2 [TRP 23 and HIE 113]	10 [Van der Waals (LYS 24, ASP 46, VAL 50, LYS 80, TRP 114, SER162, ASN 163, GLN 186, ILE 263 and LEU 303), 3 pi-pi stacked (TYR 51, TRP 82, TYR 212), 3 pi-alkyl (HIE 113, TYR 212 and CYS 301) and 2 pi-sulfur (HIE 113, PHE 125)]
			DPP-4
CMA	13	5 [GLU 168, TYR 219, PRO 513, ASP 626, and ASN 673]	7 [Van der Waals (TRP 164, TYR 510, GLY 512, CYS 514, SER 593, TYR 625 and TYR 629) and 1 pi-pi T-shaped (PHE 320)]
SGT	16	3 [GLU 168, TYR 510, and ASN 673]	8 [Van der Waals (GLU 169, SER 172, PHE 320, ARG 321, SER 593, TYR 594, TRP 622, and VAL 674), 4 pi-pi alkyl (VAL 619, TYR 625, TYR 629, and HID 703) and 1 pi-anion (GLU 168)]
			PTP1B
HDA	11	2 [ARG 56 and LYS 58]	5 [Van der Waals (PHE 30, ASP53, SER 55, LYS 73, and LYS 255), 4 pi-pi alkyl bonds (HIS 54, LEU 71 and 2 at PHE 256)]
URS	12	-	8 [Van der Waals (PRO 88, MET 113, ALA 121, GLN 122, GLN 126, MET 132, ILE 133, and ASP 136) and 4 pi-pi alkyl interactions (CYS 91, LEU 118, and 2 at 134)
			SDH
HDJ	22	5 [GLY 45, SER 46, 2 (THR 121) and ARG 298)	12 Van der Waals [(CYS 44, HIS 49, TYR 50, CYS 119, GLU 155, PRO 156, VAL 159, ILE 183, VAL 272, VAL 296, PHE 295 and TYR 299), 1 pi-pi stacked (PHE 59) and four pi-alkyl (ILE 56, HIS 69, PHE 119 and LEU 274)]
HPS	9	2 [GLY 45 and THR 250]	5 [Van der Waals (CYS 44, SER 46, HIE 49, ILE 56 and CYS 249) and 2 pi-alkyl bonds (ILE 183 and LEU 274)]

AA: alpha-amylase; AG: alpha-glucosidase; AR: aldose reductase; DPP-4: dipeptidyl peptidase-4; PTP1B: protein tyrosine phosphatase 1B; SDH: sorbitol dehydrogenase; BHP: (R)-7-butyl-6,8-dihydroxy-3-[(3e)-pent-3-en-1-yl]-3,4-dihydroisochromen-1-one; ACA: acarbose; VBG: 1-O-vanilloyl-beta-D-glucose; MGN: methyl geranate; HDJ: (-)-11-hydroxy-9,10-dihydrojasmonic acid 11-beta-D-glucoside; EPA: epalrestat; CMA: p-coumaroyl malic acid; SGT: sitagliptin; HDA: 2-hydroxydecanedioic acid; URS: ursolic acid; HPS: 4-[2-1R-hydroxy-ethyl)-pyrimidin-4- yl]piperazine-1-sulfonic acid dimethylamide.

Online First

The combination of molecular docking and MD simulation provides a comprehensive understanding of the molecular interactions and conformational changes that occur from the binding of a ligand to a target protein [81]. The MM/GBSA method calculates ΔG_{bind} for macromolecules by combining molecular mechanics calculations and continuum solvation models [82]. Lower ΔG_{bind} values align with a higher binding affinity of a ligand to a given target [83], reflecting a more stable complex [84]. The high negative ΔG_{bind} values for BHP, VBG, HDJ, CMA, HDA, and HDJ among the top investigated CS metabolites indicate a greater binding affinity to AA, AG, AR, DPP-4, PTP1B, and SDH, respectively, and potentially stronger interactions between the CS metabolites and the enzymes. The higher negative ΔG_{bind} of AA-acarbose relative to the top CS metabolites-AA complexes suggests better binding affinity of acarbose and potential in inhibiting AA activity. However, other top CS metabolites bound complexes with higher negative ΔG_{bind} values than their respective reference standards, highlighting superior potential to modulate their respective enzyme activity. Specifically, the top-ranked CS metabolites' ability to inhibit AA, AG, AR, DPP-4, PTP1B, and SDH suggests CS can prevent carbohydrate and glucagon-like

Table 5. The cDFT parameters of the top-ranked compounds against enzymes implicated in T2DM.

	cDFT parameters (eV)									
Ligands	**LUMO**	**HOMO**	**Energy gap**	**Ionization energy**	**Electron affinity**	**Hardness**	**Softness**	**Electronegativity**	**Chemical potential**	**Global electrophilicity**
					AA					
AES	−2.07	−6.42	4.35	2.07	6.42	2.17	0.46	4.24	−4.24	4.14
BHP	−1.19	−6.05	4.86	1.19	6.05	2.43	0.41	3.62	−3.62	2.70
CUR	−0.42	−6.43	6.01	0.42	6.43	3.01	0.33	3.43	−3.43	1.96
HPH	−2.24	−5.85	3.61	2.24	5.84	1.80	0.55	4.04	−4.04	4.53
AUS	−1.86	−6.56	4.70	1.86	6.56	2.35	0.43	4.21	−4.21	3.78
ACA	−0.89	−6.11	5.22	0.89	6.11	2.61	0.38	3.50	−3.50	2.35
					AG					
AUS	−1.86	−6.56	4.70	1.86	6.56	2.35	0.43	4.21	−4.21	3.78
GTA	−0.44	−7.72	7.29	0.44	7.72	3.64	0.27	4.08	−4.08	2.29
VBG	−1.47	−6.18	4.71	1.47	6.18	2.36	0.42	3.83	−3.83	3.11
MGN	−1.10	−6.34	5.24	1.10	6.34	2.62	0.38	3.72	−3.72	2.64
HDJ	−1.17	−6.46	5.29	1.17	6.46	2.65	0.38	3.82	−3.82	2.75
ACA	−0.89	−6.11	5.22	0.89	6.11	2.61	0.38	3.50	−3.50	2.35
					AR					
HPH	−2.24	−5.85	3.61	2.24	5.84	1.80	0.55	4.04	−4.04	4.53
BHP	−1.19	−6.05	4.86	1.19	6.05	2.43	0.41	3.62	−3.62	2.70
AES	−2.07	−6.42	4.35	2.07	6.42	2.17	0.46	4.24	−4.24	4.14
AUS	−1.86	−6.56	4.70	1.86	6.56	2.35	0.43	4.21	−4.21	3.78
HDJ	−1.17	−6.46	5.29	1.17	6.46	2.65	0.38	3.82	−3.82	2.75
EPA	−2.93	−6.13	3.21	2.93	6.13	1.60	0.62	4.53	−4.53	6.41
					DPP-4					
HDJ	−1.17	−6.46	5.29	1.17	6.46	2.65	0.38	3.82	−3.82	2.75
CTA	−2.06	−6.12	4.06	2.06	6.12	2.03	0.50	4.09	−4.09	4.12
BHP	−1.19	−6.05	4.86	1.19	6.05	2.43	0.41	3.62	−3.62	2.70
PHA	−2.30	−6.70	4.41	2.30	6.70	2.20	0.45	4.50	−4.50	4.59
CMA	−1.86	−6.12	4.26	1.86	6.12	2.13	0.47	3.99	−3.99	3.74
SGT	−1.35	−6.65	5.30	1.35	6.65	2.65	0.38	4.00	−3.99	3.01
					PTP1B					
HDA	−0.76	−7.42	6.66	0.76	7.42	3.33	0.30	4.08	−4.08	2.51
URS	−0.24	−6.10	5.85	0.24	6.10	2.93	0.34	3.17	−3.17	1.72
					SDH					
ETB	−0.63	−6.48	5.85	0.63	6.48	2.92	0.34	3.55	−3.55	2.16
CNI	−2.12	−6.57	4.46	2.12	6.57	2.23	0.45	4.35	−4.35	4.23
BLD	−1.63	−7.34	5.72	1.63	7.34	2.86	0.35	4.49	−4.48	3.52
HDJ	−1.17	−6.46	5.29	1.17	6.46	2.65	0.38	3.82	−3.82	2.75
BHP	−1.19	−6.05	4.86	1.19	6.05	2.43	0.41	3.62	−3.62	2.70
HPS	−1.79	−6.17	4.39	1.79	6.17	2.19	0.46	3.98	−3.98	3.61

HOMO: highest occupied molecular orbital; LUMO: lowest unoccupied molecular orbital; AA: alpha-amylase; AG: alpha-glucosidase; AR: aldose reductase; DPP-4: dipeptidyl peptidase-4; PTP1B: protein tyrosine phosphatase 1B; SDH: sorbitol dehydrogenase; AES: aesculin; BHP: (R)-7-butyl-6,8-dihydroxy-3-[(3e)-pent-3-en-1-yl]-3,4-dihydroisochromen-1-one; CUR: curvularol; HPH: (6e)-1-(4-hydroxyphenyl)-7-phenylhepta-4,6-dien-3-one; AUS: austricin; ACA: acarbose; GTA: glutaric acid; VBG: 1-O-vanilloyl-beta-D-glucose; MGN: methyl geranate; HDJ: (-)-11-hydroxy-9,10-dihydrojasmonic acid 11-beta-D-glucoside; EPA: epalrestat; CTA: caffeoyl tartaric acid; PHA: phaseic acid; CMA: p-coumaroyl malic acid; SGT: sitagliptin; TDA: tetradecanedioc acid; HDA: 2-hydroxydecanedioic acid; MCA: methylisocitric acid; DCA: dodecanedioc acid; URS: ursolic acid; ETB: erythronolide B; CNI: cnicin; BLD: blennin D; HPS: 4-[2-1R-hydroxy-ethyl)-pyrimidin-4- yl]piperazine-1-sulfonic acid dimethylamide.

Online First

Table 6. Toxicity prediction of the top ranked compounds profiled against the enzymes implicated in T2DM.

Compounds	LD_{50} (mg/kg)/TC	HT	CDT	CRG	IT	MG	CYT
AES	4000/5	In	In	In	Ac	In	In
BHP	2260/5	In	In	In	Ac	In	In
CUR	37/2	In	Ac	In	Ac	In	Ac
HPH	2000/4	In	In	In	In	In	In
AUS	125/3	In	In	Ac	In	In	In
GTA	2750/5	In	In	In	In	In	In
VBG	2260/5	In	Ac	In	In	In	In
MGN	5000/5	In	In	In	In	In	In
HDJ	10000/6	In	Ac	In	In	In	In
CTA	2000/4	In	In	Ac	In	In	In
PHA	1624/4	In	In	In	In	In	In
CMA	5000/5	In	In	In	In	In	In
TDA	900/4	In	In	In	In	In	In
HDA	3400/5	In	In	In	In	In	In
MCA	50/3	In	In	In	In	In	In
DCA	900/4	In	In	In	In	In	In
ETB	5000/5	In	In	In	Ac	In	In
CNI	452/4	In	In	In	Ac	In	In
BLD	1330/4	In	In	In	Ac	Ac	In
ACA	24000/6	Ac	Ac	In	Ac	In	In
EPA	5/2	In	In	In	In	In	In
SGT	2500/5	In	In	In	In	In	In
URS	2000/4	Ac	Ac	Ac	Ac	In	In
HPS	3000/5	In	In	In	In	In	In

AES: aesculin; BHP: (R)-7-butyl-6,8-dihydroxy-3-[(3e)-pent-3-en-1-yl]-3,4-dihydroisochromen-1-one; CUR: curvularol; HPH: (6e)-1-(4-hydroxyphenyl)-7-phenylhepta-4,6-dien-3-one; AUS: austricin; ACA: acarbose; GTA: glutaric acid; VBG: 1-O-vanilloyl-beta-D-glucose; MGN: methyl geranate; HDJ: (-)-11-hydroxy-9,10-dihydrojasmonic acid 11-beta-D-glucoside; EPA: epalrestat; CTA: caffeoyl tartaric acid; PHA: phaseic acid; CMA: p-coumaroyl malic acid; SGT: sitagliptin; TDA: tetradecanedioc acid; HDA: 2-hydroxydecanedioic acid; MCA: methylisocitric acid; DCA: dodecanedioc acid; URS: ursolic acid; ETB: erythronolide B; CNI: cnicin; BLD: blennin D; HPS: 4-[2-1R-hydroxy-ethyl)-pyrimidin-4- yl]piperazine-1-sulfonic acid dimethylamide; LD: Lethal dose; TC: Toxicity class, HT: Hepatotoxicity, CDT: Cardiotoxicity, CRG: Carcinogenity, IT: Immunotoxicity, MG: Mutagenicity, CYT: Cytotoxicity, In: Inactive, Ac: Active.

peptide 1 breakdown, enhance insulin signalling, and reduce sorbitol and fructose accumulation in cells. These effects contribute to CS's antidiabetic action by modulating enzymes involved in T2DM pathogenesis and its complications.

Additionally, MD simulation can be used to elucidate the extent of binding stability, flexibility, and compactness of a protein-ligand bound complex [11]. This is crucial due to the potential likelihood of an impending conformational or structural change that could occur after ligand binding to a receptor, which could potentially impact the biological activity of the enzyme [85,86]. The RMSD provides insight into the deviation or changes in the position of atoms over a simulation period and evaluates the stability of a protein-ligand complex [87]. A decrease in the RMSD value of a complex in comparison to the apo-enzyme throughout a simulation indicates enhanced stability [88]. The lowest mean RMSD values observed in AA-AES, AR-BHP, DPP-CTA, PTP1B-MCA, and SDH-ETB complexes in comparison to their respective apo-enzyme and reference standard complexes suggest that the binding of these CS metabolites formed stable complexes with the enzymes. Although the average RMSD values of AES and AUS were greater than the apo enzymes (AA and AG, respectively), this finding did not indicate the formation of unstable complexes since the values recorded were lower than the acceptable 3.0 Å, and hence depicting stable complexes formation [89,90]. It is noteworthy that the less stable complexes formed by the reference standards relative to the top-ranked metabolites against most of the targets in this study is in line with previous studies where compounds such as procyanidin, rutin, apigenin, chlorogenic acid, naringenin, luteolin and isoflavone bound systems exhibited lower mean RMSD values relative to their apo-enzymes and reference standards [8,11,91,92].

The RMSF of a protein-ligand system signifies the effect of a bound compound on the behavior of active site residues [93], with lower or higher shifts in alpha (α)-carbon (C) indicating less or more flexible movements, respectively [94]. Higher RMSF values signify more flexible movement and the potential of the targets to undergo conformational changes. However, the low mean RMSF values of the AA-CUR, AG-AUS, AR-BHP, DPP-4-CMA, DPP-PHA, PTP1B-MCA, and SDH-BLD complexes compared to the apo-enzyme and reference standards suggest lesser flexible movements and, consequently, greater stability and lower conformational changes in the investigated complexes. This finding agrees with previous studies for some metabolite profiled against AG and DPP-4 [11,21].

The ROG measures the spatial distribution or compactness of a molecule [95]. It calculates the average distance of individual atoms (or groups of atoms) in a molecule from its center of mass, offering insights into how spread out or condensed a molecule is during a simulation [96], with lower values indicating more compactness and thus more stability of the final complexes [97]. The CS metabolites bound to the investigated targets, specifically AA-BHP, AR-BHP, DPP-CTA, and PTP1B-MCA, exhibited the least average ROG values, suggesting a higher degree of compactness and, consequently, superior stability of the final complexes compared to the apo-enzyme and the respective standards for potential regulation of the enzyme activity. In tandem with this study, Sabiu *et al*. [21], Rampadarath *et al*. [92], and Eawsakul *et al*. [98] previously reported that the binding of the CS metabolites to AA, PTP1B, and AG, respectively, resulted in lower mean ROG in comparison to the apo-enzyme and reference standard. This observation further highlights the ability of CS metabolites to reduce the compactness and thus improve the stability of the final complexes.

Hydrogen bonds are important interactions and are essential for molecular recognition, maintaining structural stability, facilitating enzyme catalysis, influencing drug partition, and permeability [97,99]. The increase in the average number of hydrogen bonds within the complexes AA-AES, AR-BHP, DPP-BHP, PTP1B-HDA, and SDH-BLD, relative to the apo-enzyme

Online First

and standard complexes, suggests the ability of CS compounds to occupy a portion of the proteins' intramolecular phase. This results in the formation of more stable final complexes. This finding agrees with Rampadarath *et al*. [92] and Sajal *et al.* [100] studies, where they show that the binding of plant metabolites, such as β-pinene, dehydro-p-cymene, -α-pinene, orientin, vitexin, and apigenin, to DPP-4 and PTP1B presented a higher number of hydrogen bonds, in comparison to their reference standards. Hence, this suggests that CS metabolites have the potential to form a greater number of hydrogen bonds when bound to the enzyme targets better than the respective standards.

The SASA serves as a measure of thermodynamic stability, quantifying the surface area of a biomolecule available to solvent molecules [101], as well as changes in protein surface area [102]. High SASA values indicate expansion of the surface area, while lower SASA values suggest a reduction in protein volumes [97]. Apo-enzymes with higher SASA values possess greater solvent accessibility potential, which may alter their catalytic activities. The low SASA values observed in: AG-VBJ, AR-BHP, DPP-4-PHA, PTP1B-MCA, and SDH-HDJ complexes relative to the apo-enzymes and reference standard-complexes depict a higher degree of protein folding and, consequently, the formation of more stable final complexes. Similar studies also reported a reduction in SASA upon the binding of plant metabolites to the apo-enzyme [11,91,103].

In addition, the nature and number of interactions formed upon the binding of ligand and the amino acid residues of the target protein are crucial in determining the extent of the binding affinity [21]. The high number of interactions between AG-VBG, AR-HDJ, and SDH-HDJ indicated stronger and more stable ligand–protein complexes, suggesting greater interaction between the CS metabolites and target enzymes. This suggests a higher degree of inhibition of the enzymes by the CS metabolites in comparison to the reference standards. The higher negative ΔG_{bind} could be attributed to the higher number of interactions occurring between the top-ranked CS metabolites and the enzyme targets, in comparison to the reference standards investigated. While BHP and CMA did not establish more interactions when bound to AA and DPP-4, respectively, the ΔG_{bind} of the complexes formed with the CS metabolites was lower when compared to the ΔG_{bind} of the standards. This suggests that despite a lower number of interactions within the CS metabolite and enzyme complexes, the interactions formed between the complexes resulted in greater binding affinity, forming stable final complexes [84]. In contrast, the decrease in the number of interactions observed between PTP1B-HDA could contribute to the reduction in the ΔG_{bind} displayed by the complex in comparison to the URS.

The molecular characteristics of the top-ranked compounds were computed using cDFT parameters to explore their potential therapeutic importance. The HOMO and LUMO orbitals are generally recognized as important markers for forecasting the chemical and biological reactivity of chemical species [104]. The HOMO is the highest orbital that contains electrons from which electrons are transferred to the protein, forming a bond that obstructs the active site of the protein implicated in the disease condition pathogens. On the other hand, the LUMO refers to the lowest unoccupied orbital located in the innermost region that lacks electrons and functions as an electron acceptor or positive charge carrier, facilitating the transfer of these particles to larger components [105]. Therefore, investigating the HOMO and LUMO energies of lead compounds may provide crucial insights into their chemical reactivities [106].

The energy gap (ΔE) between LUMO and HOMO is essential for comprehending the reactivity, kinetic stability, and chemical characteristics of a compound [107], with a wide energy gap suggesting firmness and low chemical reactivity, whereas a small energy gap indicates softness and high chemical reactivity [108]. Unfortunately, the lower energy gaps, higher chemical softness, and lower chemical hardness against each of the targets observed by some of the top-ranked compounds did not correlate with their free binding energy, and this could be due to the observed relative residue fluctuations and increased surface area of the targets upon ligand binding. This could have reduced the effect of the reactivity of each compound on the binding free energy. This observation contradicts our previous report [41], where there is a correlation between a lower energy gap and higher negative binding free energy; however, it is consistent with Rampadarath *et al*. [106], where the lower energy gap of formoxanthone B did not result in higher negative free binding energy upon binding for MMP1.

Notably, chemical descriptors do not usually present a direct relationship with thermodynamic stability or reactivity, as shown by ΔG. Therefore, the observed ΔE and ΔG discrepancies in this study allude to the fact that ΔE and ΔG give complementary but distinct insights, and their differences might be reflecting the different aspects of molecular behavior they describe. The electrophilicity index quantifies the electrophilic reactivity of compounds. Molecules with values below 0.8 eV are categorized as weak electrophiles; values above 1.5 eV signify strong electrophiles, while between 0.8 and 1.5 eV suggest moderate electrophiles [109]. Remarkably, all the top-ranked compounds had an electrophilicity index above 1.5 eV, suggesting they are strong electrophiles with a significant electrophile presence around the molecules.

Toxicity analysis helps in predicting the degree of safety of a compound; it indicates the minimum tolerable dose in half of a population and whether a compound has the potential to cause organ or end point toxicities [21]. Generally, except for curvularol, austricin, and methyl isocitric acid, the other top compounds demonstrated relatively high tolerable doses and no organ and endpoint toxicities. This denotes little or no potential to cause pathological conditions such as inflammation, neurodegenerative diseases, T2DM, aging, cardiovascular diseases, organ disorders, and cancers [110]. While most of the compounds indicate being strong electrophiles, the electrophilicity index is a theoretical descriptor of chemical reactivity and not a direct biological or systemic toxicity predictor, as better presented by ProTox prediction; hence, the compounds demonstrate relatively safe profiles under physiologic conditions. Altogether, this study shows that CS contains a hub of metabolites; the lack of validation studies is a limitation in the work; thus, further wet-lab studies, such as *in vitro* and *in vivo* investigations to establish CS metabolites' full potential in diabetes management, are required.

Online First

5. CONCLUSION

The study established that the abundance and types of metabolites present in CS were influenced by growth stages, processing condition, and solvent polarity, with the mature CS and hydro-ethanolic extract of mature CS exhibiting higher metabolites' concentrations. The MD simulation of the metabolites over a 120-ns period against the respective enzymes profiled revealed (R)-7-butyl-6,8-dihydroxy-3-[(3e)-pent-3-en-1-yl]-3,4-dihydroisochromen-1-one (BHP), 1-O-vanilloyl-beta-D-glucose, (-)-11-hydroxy-9,10-dihydrojasmonic acid 11-beta-D-glucoside, p-coumaroyl malic acid, 2-hydroxydecanedioic acid, and (-)-11-hydroxy-9,10-dihydrojasmonic acid 11-beta-D-glucoside as potential candidates that could modulate the specific activity of alpha-amylase, alpha-glucosidase, aldose-reductase, dipeptidyl peptidase-4, protein tyrosine phosphatase 1B, and sorbitol dehydrogenase, respectively. These observations have lent scientific credence to understanding the antidiabetic mechanism of action of CS through modulation of the activity of the key enzymes involved in T2DM pathogenesis and its secondary complications, furthering the support of CS development as an antidiabetic therapeutic. However, further pre-clinical and clinical studies on the identified CS metabolites are highly suggested to establish their safety and enhance the development of CS as a potential alternative in the management of T2DM and its complications.

6. AUTHOR CONTRIBUTIONS

All authors made substantial contributions to conception and design, acquisition of data, or analysis and interpretation of data; took part in drafting the article or revising it critically for important intellectual content; agreed to submit to the current journal; gave final approval of the version to be published; and agree to be accountable for all aspects of the work. All the authors are eligible to be an author as per the International Committee of Medical Journal Editors (ICMJE) requirements/guidelines.

7. FINANCIAL SUPPORT

The authors specially acknowledge the financial assistance of the Directorate of Research and Postgraduate Support, Durban University of Technology, the National Research Foundation's (NRF) Competitive Programme for Rated Researchers Support (SRUG2204193723) and the International Centre for Genetic Engineering and Biotechnology (ZAF/HDI/CRP/024) provided to S. Sabiu. The views and opinions expressed in this paper are those of the authors and do not necessarily represent the official views of the funders.

8. CONFLICTS OF INTEREST

The authors report no financial or any other conflicts of interest in this work.

9. ETHICAL APPROVALS

This study does not involve experiments on animals or human subjects.

10. DATA AVAILABILITY

All data generated and analyzed are included in this research article.

11. PUBLISHER'S NOTE

All claims expressed in this article are solely those of the authors and do not necessarily represent those of the publisher, the editors and the reviewers. This journal remains neutral with regard to jurisdictional claims in published institutional affiliation.

12. USE OF ARTIFICIAL INTELLIGENCE (AI)-ASSISTED TECHNOLOGY

The authors declares that they have not used artificial intelligence (AI)-tools for writing and editing of the manuscript, and no images were manipulated using AI.

13. SUPPLEMENTARY MATERIAL

The supplementary material can be accessed at the journal's website: Link here [https://japsonline.com/admin/php/uploadss/4705_pdf.pdf].

REFERENCES

1. Pheiffer C, Pillay-van Wyk V, Joubert JD, Levitt N, Nglazi MD, Bradshaw D. The prevalence of type 2 diabetes in South Africa: a systematic review protocol. BMJ Open. 2018;8(7):e021029. doi: https://doi.org/10.1136/bmjopen-2017-021029
2. Yagasaki K, Muller CJF. The effect of phytochemicals and food bioactive compounds on diabetes. Int J Mol Sci. 2022;23(14):7765. doi: https://doi.org/10.3390/ijms23147765
3. Xiao E, Luo L. Alternative therapies for diabetes: a comparison of western and Traditional Chinese medicine (TCM) approaches. Curr Diabetes Rev. 2018;14(6):487–96. doi: https://doi.org/10.2174/1573399813666170519103230
4. Kharroubi AT, Darwish HM. Diabetes mellitus: the epidemic of the century. World J Diabetes. 2015;6(6):850–67. doi: https://doi.org/10.4239/wjd.v6.i6.850
5. Lin X, Xu Y, Pan X, Xu J, Ding Y, Sun X, *et al*. Global, regional, and national burden and trend of diabetes in 195 countries and territories: an analysis from 1990 to 2025. Sci Rep. 2020;10(1):14790. doi: https://doi.org/10.1038/s41598-020-71908-9
6. Animaw W, Seyoum Y. Increasing prevalence of diabetes mellitus in a developing country and its related factors. PLoS One. 2017;12(11):e0187670. doi: https://doi.org/10.1371/journal.pone.0187670
7. International Diabetes Federation (IDF) 2023. [cited 2023 August 05] Available from: https://idf.org/about-diabetes/type-2- diabetes/
8. Sabiu S, Balogun FO, Amoo SO. Phenolics profiling of *Carpobrotus edulis* (L.) N.E.Br. and insights into molecular dynamics of their significance in type 2 diabetes therapy and its retinopathy complication. Molecules. 2021;26(16):4867. doi: https://doi.org/10.3390/molecules26164867
9. Gilbert MP, Pratley RE. GLP-1 analogs and DPP-4 inhibitors in type 2 diabetes therapy: review of head-to-head clinical trials. Front Endocrinol (Lausanne). 2020;11:178. doi: https://doi.org/10.3389/fendo.2020.00178
10. Thareja S, Aggarwal S, Bhardwaj TR, Kumar M. Protein tyrosine phosphatase 1B inhibitors: a molecular level legitimate approach for the management of diabetes mellitus. Med Res Rev. 2012;32(3):459–517. doi: https://doi.org/10.1002/med.20219
11. Balogun FO, Singh K, Rampadarath A, Akoonjee A, Naidoo K, Sabiu S. Cheminformatics identification of modulators of key carbohydrate-metabolizing enzymes from *C. cujete* for type-2 diabetes mellitus intervention. J Diabetes Metab Disord. 2023;22(2):1299–317. doi: https://doi.org/10.1007/s40200-023-01249-7
12. Ramana KV. ALDOSE REDUCTASE: new insights for an old enzyme. Biomol Concepts. 2011;2(1–2):103–14. doi: https://doi.org/10.1515/BMC.2011.002

Online First

13. Moemen LA, Abdel Hamid MA, Wahab SA, Kenawy MKM, Abuelela MH, Hassanin OA, *et al*. Role of advanced glycation end products and sorbitol dehydrogenase in the pathogenesis of diabetic retinopathy. Bull Nat Res Centre. 2020;44:1–11. doi: https://doi.org/10.1186/s42269-020-00304-0
14. Sabiu S, O'Neill FH, Ashafa AOT. Toxicopathological evaluation of a 28-day repeated dose administration of *Zea mays* L. (*Poaceae*), *Stigma maydis* aqueous extract on key metabolic markers of Wistar rats. Trans R Soc S Afr. 2017;72:225–33. doi: https://doi.org/10.1080/0035919X.2017.1342713
15. Tang WH, Martin KA, Hwa J. Aldose reductase, oxidative stress, and diabetic mellitus. Front Pharmacol. 2012;3:87. doi: https://doi.org/10.3389/fphar.2012.00087
16. Omotosho IO, Obisesan OB, Oluleye O. Sorbitol dehydrogenase activity in diabetes mellitus and cataract patients. J Appl Med Sci. 2014;3:61.
17. Oboh G, Isaac AT, Akinyemi AJ, Ajani RA. Inhibition of key enzymes linked to type 2 diabetes and sodium nitroprusside induced lipid peroxidation in rats' pancreas by phenolic extracts of avocado pear leaves and fruit. Int J Biomed Sci. 2014;10(3):208–16.
18. Sharma P, Joshi T, Joshi T, Chandra S, Tamta S. Molecular dynamics simulation for screening phytochemicals as α-amylase inhibitors from medicinal plants. J Biomol Struct Dyn. 2021;39(17):6524–38. doi: https://doi.org/10.1080/07391102.2020.1801507
19. Sharma P, Singh S, Thakur V, Sharma N, Grewal AS. Novel and emerging therapeutic drug targets for management of type 2 diabetes mellitus. Obes Med. 2021;23:100329. doi: https://doi.org/10.1016/j.obmed.2021.100329
20. Thakur S, Gupta SK, Ali V, Singh P, Verma M. Aldose reductase: a cause and a potential target for the treatment of diabetic complications. Arch Pharm Res. 2021;44(7):655–67. doi: https://doi.org/10.1007/s12272-021-01343-5
21. Lukman HY, Aribisala J, Akoonjee A, Sulyman A, Wudil A, Sabiu S. Modulation of dipeptidyl peptidase by Rooibos tea metabolites towards type 2 diabetes care: evidence from molecular dynamics simulation and density functional theory. Sci Afr. 2024;2024:e02173. doi: https://doi.org/10.1016/j.sciaf.2024.e02173
22. Zhong Z, Chen Z, Liu J, Hirad AH, Sun J. *In silico* studies, antioxidant properties, antisorbitol dehydrogenase, anti-alpha amylase and anti-gastrointestinal cancer potential of violanthin as a natural compound. J Oleo Sci. 2023;72(11):1015–26. doi: https://doi.org/10.5650/jos.ess23078
23. Su J, Luo Y, Hu S, Tang L, Ouyang S. Advances in research on type 2 diabetes mellitus targets and therapeutic agents. Int J Mol Sci. 2023;24(17):13381. doi: https://doi.org/10.3390/ijms241713381
24. Lankatillake C, Huynh T, Dias DA. Understanding glycaemic control and current approaches for screening antidiabetic natural products from evidence-based medicinal plants. Plant Methods. 2019;15:105. doi: https://doi.org/10.1186/s13007-019-0487-8
25. Singh J, Inbaraj BS, Kaur S, Rasane P, Nanda, V. Phytochemical analysis and characterization of corn silk (Zea mays, G5417). Agronomy. 2022;12:777. doi: https://doi.org/10.3390/agronomy12040777
26. Singh J, Rasane P, Nanda V, Kaur S. Bioactive compounds of corn silk and their role in management of glycaemic response. J Food Sci Technol. 2023;60(6):1695–710. doi: https://doi.org/10.1007/s13197-022-05442-z
27. Sabiu S, Madende M, Ajao AAN, Ogundeji OA, Lekena N, Alayande KA. The scope of phytotherapy in southern African antidiabetic healthcare. Trans R Soc S Afr. 2019;74:1–18. doi: https://doi.org/10.1080/0035919X.2019.1575927
28. Nawaz H, Aslam M. Muntah, ST. Effect of solvent polarity and extraction method on phytochemical composition and antioxidant potential of corn silk. Free Rad Antioxid. 2019;9:5–11. doi: https://doi.org/10.5530/fra.2019.1.2
29. Wang KJ, Zhao JL. Corn silk (*Zea mays* L.), a source of natural antioxidants with α-amylase, α-glucosidase, advanced glycation and diabetic nephropathy inhibitory activities. Biomed Pharmacother. 2019;110:510–7. doi: https://doi.org/10.1016/j.biopha.2018.11.126
30. Shalihah IM, Pamela VY. Kusumasari S. Cornsilk tea extract as antidiabetic: a review. Food Sci Technol J. 2020;2(2):66. doi: https://doi.org/10.33512/fsj.v2i2.9647
31. Hasanudin K, Hashim P, Mustafa S. Corn silk (*Stigma maydis*) in healthcare: a phytochemical and pharmacological review. Molecules. 2012;17(8):9697–715. doi: https://doi.org/10.3390/molecules17089697
32. Kaur P, Singh J, Kaur M, Rasane P, Kaur S, Kaur J, *et al*. Corn silk as an agricultural waste: a comprehensive review on its nutritional composition and bioactive potential. Waste Biomass Valorisation. 2023;14:1413. doi: https://doi.org/10.1007/s12649-022-02016-0
33. Guo J, Liu T, Han L, Liu Y. The effects of corn silk on glycaemic metabolism. Nutr Metab. 2009;6:47. doi: https://doi.org/10.1186/1743-7075-6-47
34. Zhao W, Yin Y, Yu Z, Liu J, Chen F. Comparison of anti-diabetic effects of polysaccharides from corn silk on normal and hyperglycemia rats. Int J Biol Macromol. 2012;50(4):1133–7. doi: https://doi.org/10.1016/j.ijbiomac.2012.02.004
35. Chang CC, Yuan W, Roan HY, Chang JL, Huang HC, Lee YC, *et al*. The ethyl acetate fraction of corn silk exhibits dual antioxidant and anti-glycation activities and protects insulin-secreting cells from glucotoxicity. BMC Complement Altern Med. 2016;16(1):432. doi: https://doi.org/10.1186/s12906-016-1382-8
36. Vijitha TP, Saranya D. Corn silk-a medicinal boon. Int J ChemTech Res. 2017;10:129–37.
37. Haldar S, Gan L, Tay SL, Ponnalagu S, Henry CJ. Postprandial glycemic and insulinemic effects of the addition of aqueous extracts of dried corn silk, cumin seed powder or tamarind pulp, in two forms, consumed with high glycemic index rice. Foods. 2019;8:437. doi: https://doi.org/10.3390/foods8100437
38. Xu L, Zhang Y, Zhang P, Dai X, Gao Y, Lv Y, *et al*. Integrated metabolomics and network pharmacology strategy-driven active traditional Chinese medicine ingredients discovery for the alleviation of cisplatin nephrotoxicity. Chem Res Toxicol. 2019;32(12):2411–21. doi: https://doi.org/10.1021/acs.chemrestox.9b00180
39. Ran MN, Lee S. The molecular mechanisms of *Panax ginseng* in treating type 2 diabetes mellitus: network pharmacology analysis and molecular docking validation. Evid Based Complement Alternat Med. 2022;2022:3082109. doi: https://doi.org/10.1155/2022/3082109
40. Tiwari N, Thakur AK, Kumar V, Dey A, Kumar V. Therapeutic targets for diabetes mellitus: an update. Clin Pharmacol Biopharm. 2014;3:117. doi: https://doi.org/10.4172/2167-065X.1000117
41. Akoonjee A, Lanrewaju AA, Balogun FO, Makunga NP, Sabiu S. Waste to medicine: evidence from computational studies on the modulatory role of corn silk on the therapeutic targets implicated in type 2 diabetes mellitus. Biology (Basel). 2023;12(12):1509. doi: https://doi.org/10.3390/biology12121509
42. Taiwong N. Drying temperature of corn silk tea: Physical properties, total phenolic content, antioxidant activity and flavonoid content. Food Appl Biosci J. 2020;8:38.
43. Magangana TP, Makunga NP, Amos Fawole O, Opara UL. Effect of solvent extraction and blanching pre-treatment on phytochemical, antioxidant properties, enzyme inactivation and antibacterial activities of 'Wonderful' pomegranate peel extracts. Processes. 2021;9:1012. doi: https://doi.org/10.3390/pr9061012
44. Magangana TP, Makunga NP, Fawole OA, Stander MA, Opara UL. Antioxidant, antimicrobial, and metabolomic characterization of blanched pomegranate peel extracts: effect of cultivar. Molecules. 2022;27:2979. doi: https://doi.org/10.3390/molecules27092979
45. Macel M, Visschers IGS, Peters JL, Kappers IF, de Vos RCH, van Dam NM. Metabolomics of thrips resistance in pepper (*Capsicum* spp.) reveals monomer and dimer acyclic diterpene glycosides as potential chemical defenses. J Chem Ecol. 2019;45(5–6):490–501. doi: https://doi.org/10.1007/s10886-019-01074-4
46. Oh KK, Adnan M, Cho DH. Network pharmacology of bioactives from Sorghum bicolor with targets related to diabetes mellitus. PLoS One. 2020;15(12):e0240873. doi: https://doi.org/10.1371/journal.pone.0240873

Online First

47. Pettersen EF, Goddard TD, Huang CC, Couch GS, Greenblatt DM, Meng EC, *et al*. UCSF Chimera--a visualization system for exploratory research and analysis. J Comput Chem. 2004;25(13):1605–12. doi: https://doi.org/10.1002/jcc.20084
48. Akoonjee A, Lukman HY, Ajao AA, Uthman TO, Sabiu S. A network pharmacology- and molecular dynamics simulation-based bioprospection of Khaya grandifoliola C. DC. for diabetes care. J Biomol Struc Dyn. 2024;43:1–20. doi: https://doi.org/10.1080/0739110 2.2024.2446672
49. Sabiu S, Idowu K. An insight on the nature of biochemical interactions between glycyrrhizin, myricetin and CYP3A4 isoform. J Food Biochem. 2022;46(3):e13831. doi: https://doi.org/10.1111/jfbc.13831
50. Aribisala JO, Nkosi S, Idowu K, Nurain IO, Makolomakwa GM, Shode FO, *et al*. Astaxanthin-mediated bacterial lethality: evidence from oxidative stress contribution and molecular dynamics simulation. Oxid Med Cell Longev. 2021;2021:7159652. doi: https://doi.org/10.1155/2021/7159652
51. Ylilauri M, Pentikäinen OT. MMGBSA as a tool to understand the binding affinities of filamin-peptide interactions. J Chem Inf Model. 2013;53(10):2626–33. doi: https://doi.org/10.1021/ci4002475
52. Biovia DS. Discovery studio visualizer v21. 1.0. 20298. San Diego, CA: Dassault Systèmes; 2021.
53. Kruse H, Goerigk L, Grimme S. Why the standard B3LYP/6-31G* model chemistry should not be used in DFT calculations of molecular thermochemistry: understanding and correcting the problem. J Org Chem. 2012;77(23):10824–34. doi: https://doi.org/10.1021/jo302156p
54. Calais JL. Density-functional theory of atoms and molecules. RG Parr and W. Yang, Oxford University press, New York, Oxford, 1989. IX+ 333 pp. Int J Quantum Chem. 1993;47:101. doi: https://doi.org/10.1002/qua.560470107
55. Luo J, Xue ZQ, Liu WM, Wu JL, Yang ZQ. Koopmans' theorem for large molecular systems within density functional theory. J Phys Chem A. 2006;110(43):12005–9. doi: https://doi.org/10.1021/jp063669m
56. Drwal1 MN, Banerjee P, Dunkel M, Wettig MR, Preissner R. ProTox: a web server for the *in silico* prediction of rodent oral toxicity. Nucleic Acids Res. 2014;42: W53–8. doi: https://doi.org/10.1093/nar/gku401
57. Petrovska BB. Historical review of medicinal plants' usage. Pharmacogn Rev. 2012;6(11):1–5. doi: https://doi.org/10.4103/0973-7847.95849
58. Zhang Y, Wu L, Ma Z, Cheng J, Liu J. Anti-diabetic, antioxidant and anti-hyperlipidemic activities of flavonoids from corn silk on STZ-induced diabetic mice. Molecules. 2015;21(1):E7. doi: https://doi.org/10.3390/molecules21010007
59. Sripathy KV, Groot SPC. Seed development and maturation. In: Dadlani, M., Yadava, DK, editors. Seed science and technology. Springer, Singapore; 2023. doi: https://doi.org/10.1007/978-981-19-5888-5_2
60. Li R, Pan Y, Li N, Wang Q, Chen Y, Phisalaphong M, Chen H. Antibacterial and cytotoxic activities of a green synthesized silver nanoparticles using corn silk aqueous extract. Colloids Surf A: Physicochem Engineer Aspects. 2020;598:124827 doi: https://doi.org/10.1016/j.colsurfa.2020.124827
61. Sarepoua E, Tangwongchai R, Suriharn B, Lertrat K. Influence of variety and harvest maturity on phytochemical content in corn silk. Food Chem. 2015;169:424–9. doi: https://doi.org/10.1016/j.foodchem.2014.07.136 doi: https://doi.org/10.1016/j.foodchem.2014.07.136
62. Abeywardhana KW, Abeysinghe DC, Dharmadasa RM, Aththanayake AML. Determination of optimum maturity stage for *Ocimum sanctum* L. grown under different growing systems in terms of therapeutically active secondary metabolites. World J Agric Res. 2014;2:159–62. doi: https://doi.org/10.12691/wjar-2-4-4
63. Oz AT, Kafkas E. Phytochemicals in fruits and vegetables. In Waisundara V, editor. Superfood and functional food. London: IntechOpen, 2017:175–84. doi: https://doi.org/10.5772/66987
64. Haslina ME. Extract corn silk with variation of solvents on yield, total phenolics, total flavonoids and antioxidant activity. Indonesian Food Nutr Prog. 2017;14:21. doi: https://doi.org/10.22146/ifnp.24280
65. Mihali C, Frumuzachi O, Nicolescu A, Babotă M, Păltinean R, Tanase C, *et al*. Valorization of corn silk as an agricultural by-product through the optimization of ultrasound-assisted extraction. App Sci. 2024;14:1516. doi: https://doi.org/10.3390/app14041516
66. Nawaz H, Shad MA, Rehman N, Andaleeb H, Ullah N. Effect of solvent polarity on extraction yield and antioxidant properties of phytochemicals from bean (*Phaseolus vulgaris*) seeds. Braz J Pharm Sci. 2020;56:17129. doi: https://doi.org/10.1590/s2175-97902019000417129
67. Du Y, Li X, Xiong X, Cai X, Ren X, Kong Q. An investigation on polyphenol composition and content in skin of grape (*Vitis vinifera* L. cv. Hutai No.8) fruit during ripening by UHPLC-MS2 technology combined with multivariate statistical analysis. Food Biosci. 2021;43:101276. doi: https://doi.org/10.1016/j.fbio.2021.101276
68. Olennikov DN, Kashchenko NI. Componential profile and amylase inhibiting activity of phenolic compounds from *Calendula officinalis* L. leaves. Sci World J. 2014:654193. doi: https://doi.org/10.1155/2014/654193
69. Şahin H. *In-vitro* anti-diabetic, anti-Alzheimer, anti-tyrosinase, antioxidant activities of selected coumarin and dihydroisocoumarin derivatives. Int J Second Metab. 2023;10(3):361–9. doi: https://doi.org/10.21448/ijsm.1196712
70. Ononamadu CJ, Ibrahim A. Molecular docking and prediction of ADME/drug-likeness properties of potentially active antidiabetic compounds isolated from aqueous-methanol extracts of *Gymnema sylvestre* and *Combretum micranthum*. BioTechnologia. 2021;102(1):85–99. doi: https://doi.org/10.5114/bta.2021
71. Abdel-Moneim A, Yousef AI, Abd El-Twab SM, Abdel Reheim ES, Ashour MB. Gallic acid and p-coumaric acid attenuate type 2 diabetes-induced neurodegeneration in rats. Metab Brain Dis. 2017;32(4):1279–86. doi: https://doi.org/10.1007/s11011-017-0039-8
72. Mingrone G, Castagneto-Gissey L, Macé K. Use of dicarboxylic acids in type 2 diabetes. Br J Clin Pharmacol. 2013;75(3):671–6. doi: https://doi.org/10.1111/j.1365-2125.2012.04177.x
73. Bitwell C, Indra SS, Luke C, Kakoma MK. A review of modern and conventional extraction techniques and their applications for extracting phytochemicals from plants. Sci Afr. 2023;19:01585. doi: https://doi.org/10.1016/j.sciaf.2023.e01585
74. Pagadala NS, Syed K, Tuszynski J. Software for molecular docking: a review. Biophys Rev. 2017;9(2):91–102. doi: https://doi.org/10.1007/s12551-016-0247-1
75. Pantsar T, Poso A. Binding affinity via docking: fact and fiction. Molecules. 2018;23(8):1899. doi: https://doi.org/10.3390/molecules23081899
76. Pellicani F, Dal Ben D, Perali A, Pilati S. Machine learning scoring functions for drug discovery from experimental and computer-generated protein-ligand structures: towards per-target scoring functions. Molecules. 2023;28(4):1661. doi: https://doi.org/10.3390/molecules28041661
77. Agarwal S, Mehrotra RJJC. An overview of molecular docking. JSM Chem. 2016;4:1024.
78. Gupta M, Sharma R, Kumar A. Docking techniques in pharmacology: how much promising? Comput Biol Chem. 2018;76:210–7. doi: https://doi.org/10.1016/j.compbiolchem.2018.06.005
79. Lanrewaju AA, Enitan-Folami AM, Nyaga MM, Sabiu S, Swalaha FM. Metabolites profiling and cheminformatics bioprospection of selected medicinal plants against the main protease and RNA-dependent RNA polymerase of SARS-CoV-2. J Biomol Struct Dyn. 2024;42(13):6740–60. doi: https://doi.org/10.1080/07391102.2023.2236718
80. Chaudhary RK, Karoli SS, Dwivedi PSR, Bhandari R. Anti-diabetic potential of Corn silk (*Stigma maydis*): An *in-silico* approach. J Diabetes Metab Disord. 2022;21(1):445–54. doi: https://doi.org/10.1007/s40200-022-00992-7
81. Hollingsworth SA, Dror RO. Molecular dynamics simulation for all. Neuron. 2018;99(6):1129–43. doi: https://doi.org/10.1016/j.neuron.2018.08.011

Online First

82. Hou T, Wang J, Li Y, Wang W. Assessing the performance of the MM/PBSA and MM/GBSA methods. 1. The accuracy of binding free energy calculations based on molecular dynamics simulations. J Chem Inf Model. 2011;51(1):69–82. doi: https://doi.org/10.1021/ci100275a
83. Hata H, Phuoc Tran D, Marzouk Sobeh M, Kitao A. Binding free energy of protein/ligand complexes calculated using dissociation parallel cascade selection molecular dynamics and Markov state model. Biophys Physicobiol. 2021;18:305–16. doi: https://doi.org/10.2142/biophysico.bppb-v18.037
84. Shunmugam L, Soliman, ME. Targeting HCV polymerase: a structural and dynamic perspective into the mechanism of selective covalent inhibition. RSC Adv. 2018;8:42210. doi: https://doi.org/10.1039/c8ra07346e
85. Salim B, Said G, Kambouche N, Kress S. Identification of phenolic compounds from nettle as new candidate inhibitors of main enzymes responsible on type-II diabetes. Curr Drug Discov Technol. 2020;17(2):197–202. doi: https://doi.org/10.2174/1570163815666180829094831
86. Lanrewaju AA, Enitan-Folami AM, Nyaga MM, Sabiu S, Swalaha FM. Cheminformatics bioprospection of selected medicinal plants metabolites against trypsin cleaved VP4 (spike protein) of rotavirus A. J Biomol Struct Dyn. 2024;42(20):10652–71. doi: https://doi.org/10.1080/07391102.2023.2258405
87. Muralidharan N, Sakthivel R, Velmurugan D, Gromiha MM. Computational studies of drug repurposing and synergism of lopinavir, oseltamivir and ritonavir binding with SARS-CoV-2 protease against COVID-19. J Biomol Struct Dyn. 2021;39(7):2673–78. doi: https://doi.org/10.1080/07391102.2020.1752802
88. Childers MC, Daggett V. Insights from molecular dynamics simulations for computational protein design. MSDE. 2017;2:9–33. doi: https://doi.org/10.1039/C6ME00083E
89. Rosenberg MS. Sequence alignment: methods, models, concepts and strategies. Berkeley, CA: University of California Press, 2009. https://doi.org/10.1525/9780520943742
90. Castro-Alvarez A, Costa AM, Vilarrasa J. The performance of several docking programs at reproducing protein-macrolide-like crystal structures. Molecules. 2017;22(1):136. doi: https://doi.org/10.3390/molecules22010136
91. Mpofana N, Peter C, Lukman HY, Makgobole MU, Dlova NC, Gqaleni N, *et al*. Mechanisms of selected cassipourea metabolites for melasma treatment: network pharmacology and molecular dynamics study. F1000Res. 2024;13:952. doi: https://doi.org/10.12688/f1000research.153996.1
92. Rampadarath A, Balogun FO, Pillay C, Sabiu S. Identification of flavonoid C-glycosides as promising antidiabetics targeting protein tyrosine phosphatase 1B. J Diabetes Res. 2022;2022:6233217. doi: https://doi.org/10.1155/2022/6233217
93. Hess B. Convergence of sampling in protein simulations. Phys Rev. 2002;65:031910. doi: https://doi.org/10.1103/PhysRevE.65.031910
94. Al-Khodairy FM, Khan MKA, Kunhi M, Pulicat MS, Akhtar S, Arif JM. *In silico* prediction of mechanism of Erysolin-induced apoptosis in human breast cancer cell lines. Am J Bioinform Res. 2013;3:62. doi: https://doi.org/10.5923/j.bioinformatics.20130303.03
95. Alhadrami HA, Hamed AA, Hassan HM, Belbahri L, Rateb ME, Sayed AM. Flavonoids as potential anti-MRSA agents through modulation of PBP2a: a computational and experimental study. Antibiotics. 2020;9(9):562. doi: https://doi.org/10.3390/antibiotics9090562
96. Rampogu S, Lee G, Park JS, Lee KW, Kim MO. Molecular docking and molecular dynamics simulations discover curcumin analogue as a plausible dual inhibitor for SARS-CoV-2. Int J Mol Sci. 2022;23(3):1771. doi: https://doi.org/10.3390/ijms23031771
97. S'thebe NW, Aribisala JO, Sabiu S. Cheminformatics bioprospection of sunflower seeds' oils against quorum sensing system of *Pseudomonas aeruginosa*. Antibiotics (Basel). 2023;12(3):504. doi: https://doi.org/10.3390/antibiotics12030504
98. Eawsakul K, Ongtanasup T, Ngamdokmai N, Bunluepuech K. Alpha-glucosidase inhibitory activities of astilbin contained in *Bauhinia strychnifolia* Craib. stems: an investigation by *in silico* and *in vitro* studies. BMC Complement Med Ther. 2023;23(1):25. doi: https://doi.org/10.1186/s12906-023-03857-5
99. Jairajpuri DS, Hussain A, Nasreen K, Mohammad T, Anjum F, Tabish Rehman M, *et al*. Identification of natural compounds as potent inhibitors of SARS-CoV-2 main protease using combined docking and molecular dynamics simulations. Saudi J Biol Sci. 2021;28(4):2423–31. doi: https://doi.org/10.1016/j.sjbs.2021.01.040
100. Sajal H, Patil SM, Raj R, Shbeer AM, Ageel M, Ramu R. Computer-aided screening of phytoconstituents from *Ocimum tenuiflorum* against diabetes mellitus targeting DPP4 inhibition: a combination of molecular docking, molecular dynamics, and pharmacokinetics approaches. Molecules. 2022;27(16):5133. doi: https://doi.org/10.3390/molecules27165133
101. Mousavi SS, Karami A, Haghighi TM, Tumilaar SG, Fatimawali Idroes R, Mahmud S, *et al*. *In silico* evaluation of Iranian medicinal plant metabolites as inhibitors against main protease and the receptor-binding domain of SARS-CoV-2. Molecules. 2021;26:5724. doi: https://doi.org/10.3390/molecules26185724
102. Ali SA, Hassan MI, Islam A, Ahmad F. A review of methods available to estimate solvent-accessible surface areas of soluble proteins in the folded and unfolded states. Curr Protein Pept Sci. 2014;15(5):456–76. doi: https://doi.org/10.2174/1389203715666140327114232
103. Ahmed S, Ali MC, Ruma RA, Mahmud S, Paul GK, Saleh MA, *et al*. Molecular docking and dynamics simulation of natural compounds from betel leaves (*Piper betle* L.) for investigating the potential inhibition of alpha-amylase and alpha-glucosidase of type 2 diabetes. Molecules. 2022;27(14):4526. doi: https://doi.org/10.3390/molecules27144526
104. Aihara JI. Reduced HOMO− LUMO gap as an index of kinetic stability for polycyclic aromatic hydrocarbons. J Phy Chem A. 1999;103:7487–95. doi: https://doi.org/10.1021/jp990092i
105. Ahamed FM, Chinnam S, Challa M, Kariyanna G, Kumer A, Jadoun, S, *et al.* Molecular dynamics simulation, QSAR, DFT, molecular docking, ADMET, and synthesis of Ethyl 3-((5-Bromopyridin-2-yl) Imino) butanoate analogues as potential inhibitors of SARS-CoV-2. PACs. 2023;44:1–19. doi: https://doi.org/10.1080/10406638.2023.2173618
106. Rampadarath A, Aribisala JO, Makunga NP, Mazibuko-Mbeje S, Sabiu S. Molecular bioprospection of *Helianthus annuus* L.(sunflower) cypsela for antidiabetic therapeutics through network pharmacology, density functional theory and molecular dynamics simulation. S Afr J Bot. 2023;162:72–95. doi: https://doi.org/10.1016/j.sajb.2023.08.045
107. Karabacak M, Sinha L, Prasad O, Cinar Z, Cinar M. The spectroscopic (FT-Raman, FT-IR, UV and NMR), molecular electrostatic potential, polarizability and hyperpolarizability, NBO and HOMO-LUMO analysis of monomeric and dimeric structures of 4-chloro-3,5-dinitrobenzoic acid. Spectrochim Acta A Mol Biomol Spectrosc. 2012;93:33-46. doi: https://doi.org/10.1016/j.saa.2012.02.110
108. Esha NJI, Quayum ST, Saif MZ, Almatarneh MH, Rahman S, Alodhayb A, *et al*. Exploring the potential of fluoro-flavonoid derivatives as anti-lung cancer agents: DFT, molecular docking, and molecular dynamics techniques. Int J Quantum Chem. 2024;124:e7274.
109. Domingo LR, Pérez P. The nucleophilicity N index in organic chemistry. Org Biomol Chem. 2011;9:7168–75.
110. Maida CD, Daidone M, Pacinella G, Norrito RL, Pinto A, Tuttolomondo A. Diabetes and ischemic stroke: an old and new relationship an overview of the close interaction between these diseases. Int J Mol Sci. 2022;23:2397. doi: https://doi.org/10.3390/ijms23042397

How to cite this article:
Akoonjee A, Lukman HY, Lanrewaju AA, Aladodo RA, Sabiu S. Metabolomics and cheminformatics bioprospection of corn silk against key enzymes implicated in type 2 diabetes mellitus and its complications. J Appl Pharm Sci. 2025. Article in Press.
http://doi.org/10.7324/JAPS.2026.249308

Online First